Title: Inhibiting IRE1α-endonuclease activity decreases tumor burden in a mouse model for hepatocellular carcinoma.

Authors: Nataša Pavlović[1], Carlemi Calitz[1], Kessarin Thanapirom[3], Giuseppe Mazza[3], Krista Rombouts[3], Pär Gerwins[1,2] and Femke Heindryckx[1]

Affiliations:

(1) Department of Medical Cell Biology, Uppsala University, Uppsala, Sweden

(2) Department of Radiology, Uppsala University Hospital, Uppsala, Sweden

(3) Regenerative Medicine & Fibrosis Group, Institute for Liver and Digestive Health, University College London (UCL), London, UK

Running title: Inhibiting IRE1α suppresses hepatocellular carcinoma

Impact statement: Inhibiting IRE1α decreases tumor cell proliferation and migration in HCC, therefore components of this ER-stress pathway may be therapeutically relevant for liver cancer.

Keywords: Endoplasmic reticulum stress; fibrosis; hepatic stellate cells; IRE1α; tumor-stroma interactions;

Abbreviations: αSMA - α-smooth muscle actin; ATF6α - activating transcription factor 6α, DEN – N-nitrosodiethylamine; DMEM - Dulbecco modified eagle medium; ECM – extracellular matrix, ELISA - Enzyme-Linked Immune Sorbent Assay, ER - endoplasmic reticulum; FBS - fetal bovine serum; HCC - hepatocellular carcinoma,

HNF4A - hepatocyte-nuclear-factor-4-alpha, H&E - haematoxylin-eosin; IRE1α - inositol requiring enzyme 1α; PBS – phosphate buffered saline; PERK - protein kinase RNA-like endoplasmic reticulum-kinase; RIPA - radioimmunoprecipitation assay; ROS – reactive oxygen species; TBS - tris-buffered saline; TGFβ - transforming growth factor β; UPR - unfolded protein response;

Corresponding author: Femke Heindryckx, Department of Medical Cell Biology, BOX 571, Husargatan 3, 75123 Uppsala, Sweden. Phone: +46768542025 Email: femke.heindryckx@mcb.uu.se

ABSTRACT

Hepatocellular carcinoma (HCC) is a liver tumor that usually arises in patients with cirrhosis. Hepatic stellate cells are key players in the progression of HCC, as they create a fibrotic micro-environment and produce growth factors and cytokines that enhance tumor cell proliferation and migration. We assessed the role of endoplasmic reticulum (ER) stress in the cross-talk between stellate cells and HCC-cells. Mice with a fibrotic HCC were treated with the IRE1α-inhibitor 4μ8C, which reduced tumor burden and collagen deposition. By co-culturing HCC-cells with stellate cells, we found that HCC-cells activate IREα in stellate cells, thereby contributing to their activation. Inhibiting IRE1α blocked stellate cell activation, which then decreased proliferation and migration of tumor cells in different *in vitro* 2D and 3D co-cultures. In addition, we also observed cell-line specific direct effects of inhibiting IRE1α in tumor cells.

INTRODUCTION

Hepatocellular carcinoma (HCC) is a primary liver tumor that typically arises in a background of chronic liver disease and cirrhosis (1). One of the key players in the progression of cirrhosis to HCC is the hepatic stellate cell, which is activated during liver damage and differentiates towards a contractile myofibroblast-like cell that deposits extracellular matrix proteins (ECM), such as collagen (2). Activated stellate cells can induce phenotypic changes in cancer cells through the production of growth factors and cytokines that stimulate tumor cell proliferation and induce a pro-metastatic phenotype (3). Malignant hepatocytes secrete high levels of transforming growth factor beta (TGFβ), which can contribute to the activation of stellate cells in the nearby stroma(4-6). These activated stellate cells are then responsible for the deposition of ECM. Several of the ECM-components such as proteoglycans, collagens, laminin, and fibronectin interact with tumor cells and cells in the stroma, which can directly promote cellular transformation and metastasis (7, 8). The ECM can also act as a reservoir for growth factors and cytokines, which can be rapidly released to support the tumor´s needs. In addition, activated stellate cells contribute to a highly vascularized tumor micro-environment, by secreting pro-angiogenic molecules and by recruiting pro-angiogenic (and pro-tumoral) myeloid and lymphoid derived cell types (9). By constricting the hepatic microvasculature, they also cause hypoxia, which contributes to the angiogenic switch and can induce a more aggressive tumor phenotype (10). It is therefore not surprising that tumor cells actively secrete growth factors (such as TGFβ) to induce activation and migration of stellate cells, which creates a fibrotic environment that further supports and enhances tumor progression (2, 11, 12). Since activated stellate cells play an essential role in the onset and progression of HCC, blocking their activation has been proposed as a potential therapy for patients with HCC (13). One strategy to prevent stellate cell

activation, is by blocking the IRE1α-pathway of the unfolded protein response (UPR) (14, 15).

The UPR serves to cope with the accumulation of misfolded or unfolded proteins in the endoplasmic reticulum (ER) in an attempt to restore protein folding, increase ER-biosynthetic machinery and maintain cellular homeostasis (16). It can exert a cytoprotective effect by re-establishing cellular homeostasis, while apoptotic signaling pathways will be activated in case of severe and/or prolonged ER-stress (17). The presence of misfolded proteins is sensed *via* 3 transmembrane proteins in the ER: inositol requiring enzyme 1α (IRE1α), protein kinase RNA-like ER-kinase (PERK) and activating transcription factor 6α (ATF6α) (18). The development of solid tumors is characterized by uncontrolled growth and proliferation of malignant cells, resulting in a compact mass of cells and a hypoxic tumor micro-environment, two conditions that are well-characterized ER-stress inducers. Therefore, it is not surprising that activation of the UPR represents a major hallmark of several solid tumors, such as breast cancer (19), colon cancer (20) and HCC (21). The induction of the UPR in cancer cells may serve as a double-edged sword, which can aid tumor progression as well as prevent tumor growth in a context-dependent manner. Persistent ER-stress can activate pathways that induce cell death, effectively eliminating cells with a potential to become malignant. On the other hand, tumor cells may hijack the ER-stress pathways to provide survival signals required for uncontrolled growth and eventually avoid apoptosis (22). Activation of the UPR has also been shown to affect different fibrotic diseases (23), including non-alcoholic fatty liver disease (24-26), hepatitis B-induced carcinogenesis (27) and biliary cirrhosis (28). We have previously shown that inhibiting the IRE1α-branch of the UPR-pathway using 4μ8C, blocks

TGFβ-induced activation of fibroblasts and stellate cells *in vitro* and reduces liver fibrosis *in vivo* (14). In the current study, our aim was to define the role of IRE1α in the cross-talk between hepatic stellate cells and tumor cells in liver cancer. We show that pharmacologic inhibition of the IRE1α-signaling pathway decreases tumor burden in a chemically induced mouse model for HCC. Using several *in vitro* co-culturing methods, we identified that blocking IRE1α in hepatic stellate cells prevents their activation. This then decreases proliferation and migration of tumor cells in co-cultures, in addition to the direct effect of inhibiting IRE1α in tumor cells. Our results also indicate that there are cell-line specific differences in how cells respond to IRE1α-inhibition, including differences in the IRE1α-dependent generation of reactive oxygen species.

RESULTS

Pharmacological inhibition of IRE1α reduces tumor burden in a chemically induced mouse model for HCC

Hepatocellular carcinoma was induced in mice by weekly injections with N-nitrosodiethylamine (DEN) for 25 weeks (29). From week 10, IRE1α-endonuclease activity was pharmacologically inhibited with 4μ8C. Histological analysis of liver tissue confirmed the presence of liver tumors in a fibrotic background at 25 weeks (Figure 1A). Treatment with 4μ8C significantly reduced tumor burden (Figure1B), as measured on H&E-stained liver sections (Figure1A). Stellate cell activation and liver fibrosis was quantified by Sirius Red staining (Figure 1A and 1C) and immunohistochemical staining with αSMA-antibodies (Figure 1A and 1D) on liver sections. Mice with HCC had a significant increase in the percentage of collagen (Figure 1C) and αSMA-staining (Figure 1D), compared to healthy mice. Treatment with 4μ8C restored collagen (Figure 1C) and αSMA-levels (Figure 1D and Figure 1E)

to healthy baseline levels. mRNA-expression levels of *Pcna* were determined on tumor nodules and surrounding non-tumor stromal tissue (Figure 1E). As expected, proliferation of cells was increased within the tumor itself, compared to the levels in healthy liver tissue and stromal tissue. Treatment with 4µ8C significantly decreased the levels of *Pcna*-mRNA expression within the tumor, suggesting a decrease in tumor cell proliferation. A proteomics array using the Olink Mouse Exploratory assay revealed that DEN-induced murine tumors had a significantly increased protein expression of 20 oncogenic proteins compared to healthy controls (Figure 1F and table 1). In the 4µ8C-treated group, only 11 oncogenic proteins were increased compared to healthy controls (Figure 1F and table 1). Treatment with 4µ8C also significantly reduced protein expression of two HCC promotors, PRDX5 and DDAH1 (Figure 1F and table 1).

Markers of the unfolded protein response are upregulated in HCC and mainly located in the tumor stroma.

mRNA-levels of different ER-stress-genes were measured in tumor and surrounding non-tumor tissue of mice with DEN-induced HCC (Figure 2A). *Hspa5*-mRNA-expression was increased in the surrounding non-tumor tissue of DEN-induced mice with HCC, while there was no difference within the tumor, compared to healthy controls (Figure2A and B). Western blot confirmed the increase of BIP-protein expression in DEN-induced livers, which was reduced after treatment with 4µ8C (Figure 2C). The ratio of spliced to unspliced *Xbp1*-mRNA was significantly increased in the surrounding non-tumor tissue of DEN-induced mice (Figure 2D). Treatment with 4µ8C significantly reduced the ratio of spliced to unspliced *Xbp1*-mRNA in surrounding non-tumorous stromal tissue (Figure 2D). Western blot on whole tissue

samples – containing both tumor and non-tumoral tissue – also confirmed a significant decrease of XBP1-splicing after treatment with 4μ8C (Figure 2E, F and G). Immunohistochemical straining with XBP1-antibodies against the spliced variant further demonstrate that the expression of spliced XBP1 is mainly located in the peritumoral area (Figure 2H). Spliced XBP1 was significantly increased in the DEN-induced liver tissue and treatment with 4μ8C restored these levels to a similar level as seen in healthy controls (Figure 2I). Co-staining of liver tissue with antibodies against αSMA and antibodies against spliced XBP1 (Figure 2 – Figure supplement 1A and 2A), total XBP1 (Figure 2 – Figure supplement 1B and 2B), IRE1α (Figure 2 – Figure supplement 1C and 2C), phospho-IRE1α (Figure 2 – Figure supplement 1D and 2D) and BIP (Figure 2 – Figure supplement 1E and 2E), revealed that expression of markers from the IRE1α-pathway were mainly localized within activated stellate cells in the liver, although other hepatic cell populations also expressed some of these markers. At a higher magnification (Figure 2 – Figure supplement 1F) it also becomes clear that the expression of spliced XBP1 is not only cytoplasmic but some staining appears peri-nuclear and nuclear.

A gene-set enrichment assay on microarray data from HCC-patients with fibrotic septae and without fibrotic septae showed an increase of genes involved in the UPR in the fibrotic HCC samples compared to non-fibrous HCC (Figure 3A). Several actors of the IRE1α-branch of the UPR are amongst the genes that contribute to the core-enrichment of this analysis (table 2). Immunohistochemical staining of liver biopsies from HCC-patients further confirmed presence of IRE1α-mediated ER-stress markers *BIP, PPP2R5B, SHC1* and *WIPI1* localized in the fibrotic scar tissue and near hepatic blood vessels (Figure 3B). In addition, increased expression of these

markers was significantly correlated with poor survival in patients with liver cancer (Figure 3C).

Tumor cells secrete factors that induce ER-stress in hepatic stellate cells

Hepatic stellate cell-lines (LX2) and HCC-cell lines (HepG2 and Huh7) were grown in different compartments using a transwell-assay. This confirmed that tumor cells secrete factors that induce mRNA-expression of *EIF2AK3*, *DDIT3*, *HSPA5* (Figure 4A), spliced *XBP1* (Figure 4B, C and D) and *HSPA5* (Figure 4C), as well as protein expression of p-IRE1α (Figure 4F) in hepatic stellate cells co-cultured with tumor cells, indicating the presence of ER-stress. Co-culturing also led to their activation, as measured by mRNA-expression of *ACTA2* (Figure 4F) and collagen (Figure 4G) in LX2-cells grown with HepG2 or Huh7-cells in a transwell-assay. The mRNA-expression of *ACTA2* and collagen was restored to baseline levels when 4μ8C was added to the transwell co-cultures.

De-cellularised human liver 3D-scaffolds were engrafted with hepatic stellate cells (LX2) and tumor cells (HepG2). Sirius red staining and H&E staining confirmed that that LX2-cells and HepG2-cells successfully engrafted the collagen-rich matrix of the decellularized human liver scaffolds (Figure 5A and B). Engrafting both LX2-stellate cells and HepG2-cancer cells led to a significant increase of collagen staining (Figure 5B) and mRNA-expression of collagen, *HSPA5* and spliced *XBP1* (Figure 5C) compared to scaffolds that were only engrafted with LX2-cells. Adding 4μ8C significantly decreased mRNA-expression of collagen and *HSPA5* in the LX2 and HepG2 co-cultured scaffolds (Figure 5C).

Tumor cells are important sources of TGFβ, which is a known activator of stellate cells. Surprisingly, measuring TGFβ in mono-cultures lead to undetectable levels of TGFβ in Huh7-cells and low-levels in HepG2-cells (Figure 4 – figure supplement 1A). These levels increased when LX2-cells were added to the co-cultures (Figure 4 – figure supplement 1A). Engrafting both LX2-stellate cells and HepG2-cancer cells in the human liver scaffolds, slightly increased TGFβ-levels in the medium compared to scaffolds engrafted by only one cell type, but overall no significant differences were seen (Figure 4 – figure supplement 1B). It is important to note that the baseline TGFβ-levels were markedly higher in the mono-cultured scaffolds, compared to the levels measured in cells grown in a standard 2D *in vitro* set-up (Figure 4 – figure supplement 1A). Blocking TGFβ-receptor signaling with SB-431541 significantly reduced mRNA-expression of ER-stress markers *DDIT3* (Figure 4 – figure supplement 1C), spliced *XBP1* (Supplementary figure 2D-E) and *HSPA5* (Figure 4 – figure supplement 1F) in stellate cells co-cultured with tumor cells using transwells. Adding a TGFβ-receptor-inhibitor to stellate cell – tumor cell co-cultures also reduced stellate cell activation, as measured by mRNA-expression of *ACTA2* (Figure 4 – figure supplement 1G) and collagen (Figure 4 – figure supplement 1H). This indicates that TGFβ-secretion by tumor cells could be, at least in part, responsible for activating stellate cells and for inducing the IRE1α-branch of the UPR.

Pharmacological inhibition of IRE1α decreases tumor cell proliferation in stellate cell – tumor cell co-cultures

In transwell co-culturing assays, we found that co-culturing HepG2 or Huh7-tumor cells with LX2-stellate cells significantly increased *PCNA*-mRNA-expression in

HepG2 and Huh7-tumor cell lines (Figure 6A). Adding 4μ8C significantly decreased mRNA-expression of *PCNA* in Huh7-cells grown in a transwell co-culture with LX2-cells, while not affecting *PCNA*-expression in tumor cell monocultures (Figure 6A). *PCNA*-levels in HepG2-LX2 transwell co-cultures were slightly decreased, but this was not significant. Proliferation was measured 24h after exposure to 4μ8C in tumor cells (HepG2 and Huh7) grown as mono-cultures and in co-culture with LX2-stellate cells. While 4μ8C induced a significant increase in proliferation of HepG2-monocultures, no difference was seen in LX2-monocultures and a significant decrease was seen in the HepG2-LX2 co-cultures (Figure 6B). In the Huh7 tumor cell line, 4μ8C significantly decreased cell number compared to untreated controls and a similar reduction was seen in the Huh7-LX2 co-cultures (Figure 6C). Immunohistochemical staining with antibodies against EPCAM and KI67 show that the effect on proliferation is mainly localized in the tumor cell population of these co-cultures (Figure 6D).

3D-spheroids were generated using tumor cells alone (HepG2 or Huh7) or in combination with LX2-cells. While the HepG2-spheroids experienced a lower proliferation rate when generated in combination with LX2 stellate cells (Figure 6E), there was no difference in proliferation between spheroid-monocultures and spheroid-co-cultures in the Huh7-cells (Figure 6F). Treatment with 4μ8C significantly decreased proliferation of the tumor spheroids consisting of tumor cells (Huh7 or HepG2) and stellate cells (LX2), while tumor spheroid monocultures were not affected by 4μ8C. Similarly, *PCNA*-mRNA-expression significantly increased in human liver scaffolds engrafted with HepG2 and LX2-cells, compared to those engrafted with only tumor cells (Figure 7A). Treatment with 4μ8C significantly decreased *PCNA*-mRNA-expression in the LX2+HepG2 liver scaffolds, whilst not

affecting those engrafted with only tumor cells. This further confirms our hypothesis that 4μ8C can affect tumor cell proliferation indirectly, namely by blocking the activation of stellate cells and thus impairing the interaction between tumor and stromal cells.

We measured the mRNA-expression of hepatocyte-nuclear-factor-4-alpha (*HNF4A*), which is a liver function marker that is correlated to a favorable outcome for HCC-patients (30). While co-engraftment of LX2 and HepG2-cells in the liver scaffolds only lead to a marginal increase of *HNF4*A, treatment with 4μ8C significantly increased *HNF4*A-mRNA-expression, thus suggesting an overall improvement of liver function and possibly improved prognosis (Figure 7B). Immunohistochemical staining of EPCAM and KI67, showed that the HCC-cells have successfully engrafted the entire surface of the scaffolds and that 4μ8C decreased proliferation (Figure 7C).

Pharmacological inhibition of IRE1α decreases tumor cell migration in stellate cell – tumor cell co-cultures

Co-culturing HepG2 and Huh7-tumor cells with LX2-cells in the transwell assays significantly increased mRNA-expression of the pro-metastatic marker *MMP9* in HepG2-cells (Figure 8A) and *MMP1* in HepG2 and Huh7-cells (Figure 8B). Adding 4μ8C significantly decreased the mRNA-expression of *MMP1* in HepG2+LX2 and Huh7+LX2 transwell co-cultures, while a non-significant decrease of *MMP9* mRNA-expression was seen in Huh7+LX2 transwell co-cultures. To assess whether this reduction in mRNA-expression of pro-metastatic markers has a functional effect on cell migration, a scratch wound assay was performed on confluent layers of mono-cultures (HepG2 or LX2) or tumor cell (HepG2) – stellate cell (LX2) co-cultures (Figure 8C). To visualize closing of the scratch wound by each individual cell type,

cells were fluorescently labeled using CellTracker Green (tumor cells) or CellTracker Red (LX2 stellate cells) (Figure 8D). Tumor-stellate cell co-cultures were the most efficient to close the scratch wound (Figure 8E). This was significantly inhibited when co-cultures were treated with 4μ8C. We also observed a direct effect of 4μ8C on LX2 and HepG2-migration, since treatment with 4μ8C lead to a significant reduction in wound closure after 24h, compared to untreated controls. It is important to note that traditional scratch wound assays cannot distinguish between proliferation and migration (31). To overcome this limitation (32), we counted the individual number of cells in the middle of the wound area (Figure 8F and G). No significant difference was seen between HepG2 or LX2-cells within the wound area of HepG2-LX2 co-cultures after 24 hours (Figure8F). However, 4μ8C-treatment significantly decreased migration of HepG2-cells and LX2-cells inside the scratch wound in co-cultures, while not affecting mono-cultures (Figure 8G).

Metastasis is usually a result of directed migration and chemotaxis toward physical and biochemical gradients within the tumor stroma (33). We used a microfluidic-based device for studying cell migration towards a stable gradient of chemotactic factors, such as FBS. 4μ8C significantly decreased total migration (Figure 8 – figure supplement 1A-C) and directional migration towards FBS (Figure 8 – figure supplement 1B and D) of HepG2-cells co-cultured with LX2-cells. Similarly, inhibition of IRE1α with 4μ8C significantly decreased total migration (Figure 8 – figure supplement 1E and G) and directional migration towards FBS (Figure 8 – figure supplement 1F and H) of LX2-cells co-cultured with HepG2-cells. Overall, these data suggest that stellate cells increase proliferation and pro-metastatic potential of tumor cells and blocking the IRE1α-RNase activity decreases tumor cell proliferation and migration.

Silencing of IRE1α in stellate cells decreases tumor cell proliferation and migration in co-cultures

To investigate whether the effect of blocking IRE1α is due to a direct effect on the tumor cells or because of an indirect effect via stellate cells, we transfected the stellate-line LX2 and the tumor cell lines Huh7 and HepG2 with an-siRNA targeting IRE1α, prior to co-culturing. In the LX2-cells, transfection efficiency was determined via qPCR and showed a 50% reduction in the ERN1-mRNA-expression (Figure 9A) compared to mock-transfected (Scr) controls. In the transwell co-culturing assay, we found that silencing IRE1α in the LX2-cells significantly decreased *PCNA*-mRNA-expression in HepG2-cells (Figure 9B). Silencing IRE1α in the LX2-cells also lead to a significant reduction of proliferation in LX2-HepG2 co-cultures (Figure 9C) and LX2-HepG2 spheroids (Figure 9 – figure supplement 1A). Immunocytochemical staining with αSMA-antibodies (Figure 9 – figure supplement 1B), confirmed a significant reduction of αSMA after si-IRE1α-transfection of LX2-stellate cells in HepG2-LX2 spheroid co-cultures (Figure 9 – figure supplement 1C). A scratch wound assay on HepG2-LX2 co-cultures verified that silencing of IRE1α in LX2-cells significantly reduced wound closure compared to non-transfected and mock-transfected stellate cells (Figure 9 – figure supplement 1 D - E). Overall, these data confirm that blocking the IRE1α-pathway in hepatic stellate cells decreases proliferation and pro-metastatic potential of tumor cells in co-cultures.

In the cancer-cells, transfection efficiency was determined via qPCR and showed a 40% reduction in the *ERN1*-mRNA-expression in HepG2-cells and 65% in the Huh7-cells (Figure 9D). Interestingly, we found that silencing IRE1α in the HepG2-cells led to a significant reduction of proliferation in LX2-HepG2 co-cultures and in the HepG2-

monocultures, while silencing IRE1α in the Huh7-cells led to a significant increase in both mono- and co-cultures (Figure 9E). These results indicate that silencing IRE1α in the tumor cells also directly affects tumor cell proliferation, but the effect seems to be cell line dependent.

Inhibiting IRE1α affects the generation of reactive oxygen species

To study if the observed effects of inhibiting IRE1α are through an effect on the generation of reactive oxygen species (ROS), we measured intracellular ROS-levels in 4μ8C-treated (Figure 10A) and *IRE1α*-silenced cell lines (Figure 10B). Treatment with 50 μM 4μ8C and 100 μM 4μ8C significantly decreased intracellular ROS-levels in LX2, HepG2 and Huh7-cells (Figure 10A). No differences were observed between the two concentrations (Figure 10A). In the si-IRE1α transfected cells, the effect on ROS-generation seemed to be dependent on the cell type (Figure 10B). Transfecting LX2-cells with si-IRE1α led to a significant decrease in intracellular ROS, while this caused a significant increase in the HepG2-cell line (Figure 10B). No significant differences were seen in the Huh7-cells (Figure 10B). Treatment with 4μ8C further decreased ROS-generation in all transfected cell lines (Figure 10B).

DISCUSSION

There is increasing evidence that ER-stress and activation of the UPR play an essential role during hepatic inflammation and chronic liver disease. We have previously shown that inhibition of IRE1α prevents stellate cell activation and reduces liver cirrhosis *in vivo* (14). In this report, we further define a role of the IRE1α-branch of the UPR in the interaction between tumor cells and hepatic stellate cells. We also

show that IRE1α could form a valuable therapeutic target to slow down the progression of hepatocellular carcinoma, both through the effect on stromal cells and *via* the direct effect on cancer cells.

Activated stellate cells play an important role in promoting tumorigenesis and tumors are known to secrete cytokines, such as TGFβ, which activate stellate cells and thereby creates an environment that helps to sustain tumor growth (34). Since over 80% of HCC arises in a setting of chronic inflammation associated with liver fibrosis, targeting the fibrotic tumor micro-environment is often proposed as a valuable therapeutic strategy for HCC-patients (2). We and others have shown that ER-stress plays an important role in stellate cell activation and contributes to the progression of liver fibrosis (14, 35-38). The mechanisms by which the UPR promotes stellate cell activation have been attributed to regulating the expression of c-MYB (14), increasing the expression of SMAD-proteins (35) and/or by triggering autophagy (37, 38).

In our study, we show that IRE1α plays an important role in stellate cell – tumor cell interactions and that pharmacological inhibition of IRE1α-endoribonuclease activity slows down the progression of HCC *in vivo*. We demonstrate that tumor cells can induce the IRE1α-branch of the UPR in hepatic stellate cells, thereby contributing to their activation and creating an environment that is supportive for tumor growth and metastasis. By co-culturing stellate cells with tumor cells, we mainly observed an increase of the IRE1α-branch of the UPR, however it is important to note that HepG2-cells also significantly induced mRNA-expression of *EIF2AK3*, while Huh7-cells seemed to induce *DDIT3* in the LX2-cells. These results indicate that ATF6α and PERK-pathways may also play an important role in the interaction between

stellate cells and tumor cells. In our study, we also observe that overall levels of XBP1 (spliced and unspliced) were very low in the LX2 monocultures and LX2 + HepG2 co-cultures treated with 4μ8C. This is likely the result of low baseline levels of total XBP1 in these conditions. Several studies have shown that constitutive levels of total XBP1 can be low (39) and that the levels of spliced and unspliced XBP1 can both increase during ER-stress (40-42). The conditions where we observe low levels of both unspliced and spliced XBP1 correspond to those where we expect to see low levels of IRE1α activation and thus possibly suggest that ER-stress increased the levels of total XBP1 in hepatic stellate cells. Another unexpected finding in our study is the predominant cytoplasmic localization of spliced XBP1 in liver tissue. Spliced XBP1 contains a nuclear localization signal and a transcriptional activation domain, which can activate the transcription of the UPR target genes. In our study, we do not observe a clear nuclear expression of spliced XBP1, which is in contrast to the study of Yoshida et al, which shows that spliced XBP1 predominantly localizes in the nucleus of HeLa-cells exposed to acute ER-stress (43). This study also describes a mechanism whereby unspliced-XBP1 forms a complex with the spliced isoform, thereby exporting it from the nucleus to the cytoplasm, resulting in subsequent degradation by the proteasome. However, this event has been described during the recovery phase of an acute ER-stress event. In our mouse model, we treated mice with a hepatocarcinogenic compound for 25 weeks, resulting in a chronic inflammation and a subsequent activation of IRE1α-dependent ER-stress pathways. It is therefore not unlikely that different cells in this model are experiencing different phases of ER-stress and recovery. At a higher magnification, it becomes clear that the expression of spliced XBP1 is not only cytoplasmic but some staining appears peri-nuclear and nuclear. This could represent different stages of ER-stress

activation and recovery in different cell populations; however, more experiments would be needed to verify this hypothesis.

Our results show that TGFβ-secretion by tumor cells could be in part responsible for activating stellate cells and for inducing the IRE1α-branch of the UPR. However, this seems to depend on the cell lines used, as the effect was not seen in the LX2 and HepG2 co-cultures. In these co-cultures, an autocrine signaling mechanism may be playing a role in the LX2-cells and the HepG2 cells may even prevent this. One possible alternative mechanism is through CCN protein upregulation, as this has been shown to induce ER-stress and UPR-activation in both stellate cells and hepatocytes by *in vitro* and *in vivo* approaches. CCN proteins are ECM-associated secreted proteins which play a role in a with a wide array of important functions, such as wound healing and tumorigenesis (44). Adenoviral CCN gene transfer and overexpression of CCN proteins have been shown to induce ER-stress mediated stellate cell senescence and apoptosis in later stages of fibrosis, consequently contributing to fibrosis resolution (45, 46). While ER stress is known to play a key role in stellate cell activation and hepatocyte apoptosis during the fibrosis progression, inducing ER stress-mediated apoptosis in activated stellate cells in advanced stages of fibrosis could be a relevant therapeutic strategy to attenuate liver fibrosis (45, 46).

Activated stellate cells are known to enhance migration and proliferation of tumor cells *in vitro (8)* and *in vivo* (47), by producing ECM-proteins and by secreting growth factors. Extracellular matrix proteins such as collagen can act as a scaffold for tumor cell migration (48), alter the expression of MMP´s (8) and induce epithelial-mesenchymal transition (49). Activated stellate cells are also an important source of

hepatocyte growth factor, which promotes proliferation, cell invasion and epithelial-mesenchymal transition via the c-MET signaling pathway (50). Interestingly, blocking IRE1α in the stellate cell population reduced tumor-induced activation towards myofibroblasts, which then decreases proliferation and migration of tumor-cells in co-cultures. This suggests that targeting the microenvironment using an ER-stress inhibitor could be a promising strategy for patients with HCC.

The UPR has been described as an essential hallmark of HCC (51), although its role within tumorigenesis remains controversial (21). While a mild to moderate level of ER-stress leads to activation of the UPR and enables cancer cells to survive and adapt to adverse environmental conditions, the occurrence of severe or sustained ER-stress leads to apoptosis. Both ER-stress inhibitors and ER-stress inducers have therefore been shown to act as potential anti-cancer therapies (52). A recent study by Wu *et al*, demonstrated that IRE1α promotes progression of HCC and that hepatocyte specific ablation of IRE1α results in a decreased tumorigenesis (53). In contrast to their study, we found a greater upregulation of actors of the IRE1α-branch within the stroma than in the tumor itself and identified that expression of these IRE1α-markers was mainly localized within the stellate cell population. An important difference between both studies is the mouse model that was used. While Wu *et al* used a single injection of DEN, we performed weekly injections, causing tumors to occur in a background of fibrosis, similar to what is seen in patients (29). Our *in vitro* studies with mono-cultures confirm that 4μ8C and transfection with si-IRE1α also has a direct effect on proliferation, migration and intracellular levels of ROS in HCC-cells – similar to the findings of Wu *et al* - and the response seems to depend on the tumor cell line. Adding 4μ8C to HepG2-cells significantly increased proliferation, while a

significant decrease was seen in the Huh7-cells. This difference in response could be due IRE1α´s function as a key cell fate regulator. On the one hand IRE1α can induce mechanisms that restore protein homeostasis and promote cytoprotection, while on the other hand IRE1α also activates apoptotic signaling pathways. How and when IRE1α exerts its cytoprotective or its pro-apoptotic function remains largely unknown. The duration and severity of ER-stress seems to be a major contributor to the switch towards apoptosis, possibly by inducing changes in the conformational structure of IRE1α (54). The threshold at which cells experience a severe and prolonged ER-stress that would induce apoptosis could differ between different cell lines, depending on the translational capacity of the cells (e.g. ER-size, number of chaperones and the amount of degradation machinery) and the intrinsic sources that cause ER-stress (55). A study of Li *et al*, has specifically looked at how IRE1α regulates cell growth and apoptosis in HepG2-cells (56). Similar to our findings, they discovered that inhibiting IRE1α enhances cell proliferation, while over-expression of IRE1α increases the expression of polo-like kinase, which leads to apoptosis. Interestingly, polo-like kinases have divergent roles on HCC-cell growth depending on which cell line is used, which could explain the different response to 4μ8C in Huh7 and HepG2-cells (57). Studies on glioma cells show that IRE1α regulates invasion through MMP´s (58). In line with these results, we also detected a reduction of *MMP1*-mRNA expression after 4μ8C-treatment and observed a direct effect on wound closure in HepG2-cells. These results indicate that IRE1α could play a direct role in regulating tumor cell invasion, in addition to its indirect effect via stellate cells. This is also in line with our findings that silencing IRE1α in the tumor cells affects tumor cell proliferation, although this effect seems to be cell line dependent.

Another possible mechanism that explains the cell line specific differences in response to inhibiting IRE1α, is through the generation of ROS. Studies have shown that IRE1α plays an important role in mediating ROS-generation (59) and 4μ8C has been described as a potent ROS-scavenger (60). IRE1α generates ROS through Ca^{2+}- mediated signaling between the IRE1α-InsP3R pathway in the ER and the redox-dependent apoptotic pathway in the mitochondrion, as well as *via* activation of CHOP, BIP and through XBP1-splicing (61, 62). In line with these findings, we found a significant reduction in intracellular ROS-levels after treatment with 4μ8C in LX2, HepG2 and Huh7-cells. Interestingly, a similar reduction in ROS-generation as in the 4μ8C-treated LX2-cells was seen after transfection of LX2-cells, while an increase of ROS-generation was noted in the transfected HepG2-cells. These results indicate that the reduction in ROS could partially be explained through the decreased activation of the IRE1α-pathway in the LX2-cells. However, how the IRE1α-pathway affects the generation of ROS, seems to be cell-type dependent, as we see different results in the different cell lines we tested. This is in line with previous studies, which also observed this cell line dependent effect on IRE1α-dependent ROS-generation (60, 62). The HepG2 and Huh7-cell lines used in this study are known to have different sensitivities to doxorubicin, a property that has been ascribed to their differences in intracellular ROS-generation after treatment with this chemotherapeutic agent (63). Alterations in oxidative stress can affect cell proliferation, specifically in cancer cells and stellate cells (64). In addition, ROS is one of the critical mediators of stellate cell activation and ECM-production (65). Oxidative stress has been recognized as one of the key factors in the pathogenesis of HCC and treatment strategies aiming at controlling oxidative stress have shown promising pre-clinical results (66, 67). Therefore, an IRE1α-mediated regulation of ROS-generation might

be a contributing factor that explains our findings on stellate cell activation and tumor cell proliferation after inhibiting IRE1α with 4μ8C or transfection. However, more research is necessary to further elucidate the role of IRE1α in mediating ROS-generation in different cell types. In addition, since we see a potent decrease on ROS-levels after treatment with 4μ8C, even in the cells that were transfected with si-IRE1α, we cannot exclude that – at least part – of our results could be explained through the off-target effect of 4μ8C as a ROS-scavenger. Inhibiting oxidative stress has been shown to attenuate tumor progression in different pre-clinical models for HCC and ROS is a known contributor to the chronic liver disease and HCC (68, 69). Further research is necessary to assess to which extent the ROS-scavenging effect in our study has influenced cancer progression.

In conclusion, the aim of this study was to define the role of IRE1α in the cross-talk between hepatic stellate cells and tumor cells in liver cancer. We show that pharmacologic inhibition of the IRE1α-signaling pathway decreases tumor burden in a DEN-induced mouse model for HCC. Using several *in vitro* 2D and 3D co-culturing methods, we show that tumor cells can induce the IRE1α-branch of the ER-stress pathways in hepatic stellate cells and that this contributes to their activation. Blocking IRE1α-in these hepatic stellate cells prevents their activation. This then contributes to a decreased proliferation and migration of tumor cells in co-cultures, in addition to the direct effect of inhibiting IRE1α in tumor cells. Our results indicate there are cell line specific differences in the response to IRE1α-inhibition, including intercellular variations in how blocking IRE1α affects the generation of ROS.

MATERIAL AND METHODS

522

Key Resources Table				
Reagent type (species) or resource	**Designation**	**Source or reference**	**Identifiers**	**Additional information**
strain, strain background (*Mus musculus)*	Sv129 mice	Taconic	129S6	HCC mouse model, (29, 70).
Cell line (*Homo sapiens*)	HepG2	ATCC	HB-8065™	
Cell line (*Homo sapiens*)	Huh7	Gifted, Karolinska institute		
Cell line (*Homo sapiens*)	LX2	Sigma-Aldrich	SCC064	
Transfected construct (human)	si-IRE1α	ThermoFisher	s200432	0,1 - 1 µM
Transfected construct (human)	Si-Ctrl; Scr	ThermoFisher	4390843	0,1 - 1 µM
Antibody	KI67 (rat monoclonal)	eBioscience	SolA15	1:100
Antibody	EPCAM (rabbit polyclonal)	Abcam	ab71916	1:100
Antibody	Spliced XBP1 (goat monoclonal)	Abcam	Ab85546	1:50
Antibody	Total XBP1 (Rabbit polyclonal)	Abcam	Ab37152	5 µg/ml.

Antibody	IRE1a (rabbit polyclonal)	Abcam	Ab37073	1 µg/ml.
Antibody	p-IRE1 (rabbit polyclonal)	AbNova	PAB12435	1:100
Antibody	αSMA (Rabbit Polyclonal)	ThermoFisher	710487	1:200
Antibody	αSMA (Goat monocolonal)	Abcam	Ab21027	1-2 µg/mL
Antibody	BIP (goat polyclonal)	Abcam	Ab21027	1 µg/ml
Antibody	Vinculin (Mouse monoclonal)	ThermoFisher	14-9777-82	1-5 µg/mL
peptide, recombinant protein	*Pst*-I	ThermoFisher	ER0615	
commercial assay or kit	Pierce™ BCA-protein assay kit	ThermoFisher	233225	
commercial assay or kit	EZNA® RNA isolation Kit II	VWR	R6934-02	
commercial assay or kit	RNeasy Universal Mini Kit	Qiagen	73404	
commercial assay or kit	Diva Decloacker solution	Biocare	DV2004	
commercial assay or kit	DCFDA - Cellular ROS Detection Assay Kit	Abcam	ab113851	

chemical compound, drug	N-Nitrosodiethylamine, DEN	Sigma-Aldrich	1002877809	
chemical compound, drug	4μ8C	Sigma-Aldrich	SML0949-25MG	(14)
chemical compound, drug	SB-431541, TGF-ß receptor inhibitor	Tocris	1614	10μM
chemical compound, drug	Resazurin	Sigma-Aldrich	R7017-1G	1:80 dilution
commercial assay or kit	Ingenio® electroporation solution	Mirus Bio LLC	MIR50114	Ice-cold
commercial assay or kit	CellTracker™ Red CMTPX	ThermoFisher	C34552	1μM
commercial assay or kit	CellTracker™ Green CMFDA	ThermoFisher	C2925	1μM
other	12-well Corning® Costar® Transwell® plates	Sigma-Aldrich	3460	(71)
other	Corning® Costar® Ultra-Low attachment 96-well plates	Sigma-Aldrich	CLS3471	(72)
other	CellDirector®	GradienTech	11-001-10	(73)

Mouse model

A chemically induced mouse model for HCC was used, as previously described (29, 70). Briefly, 5-week-old male Sv129 mice received intraperitoneal injections once per

week with 35mg/kg bodyweight N-Nitrosodiethylamine (DEN) (1002877809, Sigma-Aldrich, Darmstadt, Germany) diluted in saline. From week 10, mice were injected twice per week with 10µg/g bodyweight 4µ8C (SML0949-25MG, Sigma-Aldrich, Darmstadt, Germany) in saline. After 25 weeks mice were euthanized and samples were taken for analysis. The methods were approved by the Uppsala ethical committee for animal experimentation (C95/14). Each group contained 8 mice, which generates enough power to pick up statistically significant differences between treatments, as determined from previous experience (29, 70). Mice were assigned to random groups before treatment.

Sampling of animal tissue

Liver tissue for mRNA-analysis was divided in non-tumor tissue and tumor tissue, by excising macroscopically visible tumors using surgical micro-scissors. Tissue fragments were then immersed in RNA-later solution (Sigma-Aldrich, Darmstadt, Germany) and incubated on ice for 30 minutes, followed by snap freezing on dry ice and storage in -80°C. For protein analysis, liver tissue was immediately snap frozen without separating tumor and non-tumor tissue. For paraffin-embedding, half of the left liver lobe was rinsed in ice-cold saline solution and fixed in 4% paraformaldehyde for 24h.

Olink multiplex proximity extension assay

Liver samples were homogenized in ice-cold radioimmunoprecipitation assay (RIPA) buffer (20-188, Merck-Millipore, Solna, Sweden), containing Halt™ Protease inhibitor cocktail (78425, ThermoFisher Scientific, Stockholm, Sweden). Homogenates were kept on ice for 20–30 min, whilst mixing vigorously to enhance disruption of the cell membranes. The homogenates were then centrifuged (20 min,

554 13 000 rpm, 4°C) and supernatant containing protein was collected. Supernatant was
555 stored at -20°C until protein measurement. Protein concentration was measured
556 using the Pierce™ BCA-protein assay kit (233225, ThermoFisher Scientific,
557 Stockholm, Sweden) and all samples were diluted to 1 mg/mL protein in RIPA-buffer.
558 Samples from 3 biological replicates per group were analyzed with a multiplex
559 proximity extension assay for ninety-two biomarkers in the murine exploratory panel
560 (Olink Bioscience, Uppsala, Sweden) (74). Samples were loaded at random on the
561 assay plates. Raw data was deposited in Dryad (75).
562
563 *Cell culture and reagents*
564 The HCC-cell lines (HepG2, ATCC® HB-8065™ and Huh7, kind gift from Dilruba
565 Ahmed, Karolinska Institute, Sweden) and the human hepatic stellate cell-line LX2
566 (SCC064, Sigma-Aldrich, Darmstadt, Germany) were cultured at 37˚C with 5% CO_2
567 in high glucose Dulbecco modified eagle medium, GlutaMAX™ supplemented
568 (DMEM) (31066047, ThermoFisher Scientific, Stockholm, Sweden) supplemented
569 with
570 1% antibiotic antimycotic solution (A5955-100ML, Sigma-Aldrich, Darmstadt,
571 Germany) followed by 10% and 2% fetal bovine serum (FBS) (10270106,
572 ThermoFisher Scientific, Stockholm, Sweden) for the HCC cell lines and LX2 cell line
573 respectively (71). No FBS was used during starvation and stimulation with growth
574 factors. Misidentification of the three cell lines was checked at the Register of
575 Misidentified Cell Lines, and none of the chosen cell lines were on the list (76).
576 Extracted DNA from all our cell lines are sent yearly to Eurofins Genomics
577 (Ebersberg, Germany) for cell line authentication using DNA/STR-profiles.

Authentication confirmed the correct identity of each cell line and each cell line was tested negative for mycoplasma contamination.

For transwell co-culturing experiments, cells were grown on 12-well Corning® Costar® Transwell® plates (3460, Sigma-Aldrich, Darmstadt, Germany) with 0,4µm-pore polyester membrane, allowing the exchange of soluble factors, but preventing direct cell contact (71). Cells were detached using 0,05% trypsin-EDTA (15400054, ThermoFisher Scientific, Stockholm, Sweden), re-suspended in growth medium and seeded at a density of 1.0 x 10^5 cells per well and 4.0 x 10^4 cells per insert. Cells were allowed to attach and left undisturbed for 8h, followed by 16h of starvation in serum-free medium. Afterwards, fresh starvation medium containing indicated growth factors or substances were added. Cells were exposed for 48h to 50µM or 100µM 4µ8C or 10µM SB-431541 (1614, Tocris, Abingdon, UK), as previously described (14).

3D-tumor spheroids were generated in flat bottom Corning® Costar® Ultra-Low attachment 96-well plates (CLS3471, Sigma-Aldrich, Darmstadt, Germany) (72). After 6 days, spheroids had reached approximately 1mm^2 and 4µ8C was added. Proliferation was monitored during the subsequent 4 days. Tumor spheroids were retrieved from the plates after 10 days and used for immunohistochemical staining.

Human liver scaffold decellularization and cell culture usage

Human healthy livers were obtained under the UCL Royal Free BioBank Ethical Review Committee (NRES Rec Reference: 11/WA/0077) approval. Informed consent was obtained for each donor and confirmed via the NHSBT ODT organ retrieval

pathway (77). Liver 3D-scaffolds, were decellularized, sterilized and prepared for cell culture use, as previously described (77). LX2 and HepG2-cells, as either mono-cultures or mixed co-culture, were at a seeding density of 2.5 x 10^5 cells in volume of 20µL per scaffold (78).

Proliferation

Cell proliferation was monitored *via* a resazurin reduction assay (79). Cells were seeded onto Corning® 96-well, flat, clear bottom, black plates (CLS3603-48EA, Sigma-Aldrich, Darmstadt, Germany) at a seeding density of 1.0 x 10^4 cells for monocultures and a 1:1 ratio of 5.0 x 10^3 cells for co-cultures, per well. A 1% resazurin sodium salt solution (R7017-1G, Sigma-Aldrich, Darmstadt, Germany) was added in 1/80 dilution to the cells and incubated for 24h, after which fluorescent signal was measured with a 540/35 excitation filter and a 590/20 emission filter on a Fluostar Omega plate reader.

Transfections

Nucleofection with 0,1 - 1 µM si-IRE1α (s200432, ThermoFisher Scientific, Stockholm, Sweden), or 0,1 µM siCtrl (4390843, ThermoFisher Scientific, Stockholm, Sweden) was done using Amaxa Nucleofector program S-005 (LX2-cells) or T-028 (HepG2 and Huh7) in ice-cold Ingenio® electroporation solution (MIR50114, Mirus Bio LLC, Taastrup, Denmark) on 1.0 x 10^6 cells per transfection. Cells were promptly re-suspended in 2 mL DMEM with 10% FBS and left adhere for 6-8 hours, after which the medium was changed to fresh DMEM. Transfection efficiency was checked 24 hours post-transfection by qPCR. Only one si-RNA was used, as this reduced mRNA expression by >40% in all cell lines.

Migration and chemotaxis

Non-directional migration was assessed using a scratch wound assay, as previously described (80). In short, cells fluorescently labelled by using CellTracker™ dye, according to manufacturer´s instructions. Cell pellets were incubated 30 minutes with 1µM of CellTracker™ Red CMTPX (C34552, ThermoFisher Scientific, Stockholm, Sweden) or 1µM of CellTracker™ Green CMFDA (C2925, ThermoFisher Scientific, Stockholm, Sweden). Cells were washed twice in phosphate buffered saline (PBS) (P4417-100TAB, Sigma-Aldrich, Darmstadt, Germany) and seeded in 12-well plates. The cells were left to reach 100% confluency overnight, after which a scratch was created on the confluent cell layer, using a 200uL pipet tip. Medium was aspirated from each well and replaced by fresh DMEM containing 10% FBS. Invasion of cells into the scratch wound area was monitored using fluorescence microscopy images and light microscopy images. Scratch size was measured by analyzing light microscopy images in ImageJ, using the MRI Wound Healing Tool plug-in (http://dev.mri.cnrs.fr/projects/imagej-macros/wiki/Wound_Healing_Tool). Image analysis was done in ImageJ.

Directional migration was assessed using CellDirector®-devices (11-001-10 GradienTech, Uppsala, Sweden), following manufacturer´s recommendations (73). HepG2 and LX2-cells were labelled with CellTracker-dye and left to adhere overnight in the CellDirector-devices. Non-adherent cells were washed away with DMEM and cells were starved for 1h prior to commencing experiments. A gradient of 0 to 10% FBS was created with a flow rate of 1.5 µl/minute. Cell movement was recorded using an Axiovision 200M microscope (Zeiss, Stockholm, Sweden) for 4h and

652 tracked using Axiovision software (Zeiss, Stockholm, Sweden). During the assay
653 cells were kept at 37˚C with 5% CO_2.
654
655 *Quantitative RT-PCR of mRNA*
656 RNA was isolated from tissue or cell culture using the EZNA® RNA isolation Kit II
657 (R6934-02, VWR, Spånga, Sweden) or using QIAzol® lysis reagent (79306, Qiagen,
658 Sollentuna, Sweden) and RNeasy Universal Mini Kit (73404, Qiagen, Sollentuna,
659 Sweden) for human liver scaffolds (77). RNA-concentration and purity were
660 evaluated using Nanodrop. Afterwards, 500ng of mRNA was reverse transcribed
661 using iScript select cDNA synthesis kit (1708897, Bio-rad, Solna, Sweden).
662 Amplifications were done using primers summarized in supplementary table 1.
663 mRNA-expression was normalized to *18S, GAPDH* and/or *TBP1.* Fold change was
664 calculated *via* the delta-delta-CT method, by using the average CT value of 3
665 technical replicates.
666 The procedure to detect the spliced and unspliced isoforms of XBP1 was done by
667 digesting RT-PCR product with the restriction enzyme *Pst*-I (ER0615, ThermoFisher
668 Scientific, Stockholm, Sweden). This cleaves unspliced-XBP1 containing the *Pst*-I-
669 cleavage site (CTGCA^G), but leaves the spliced isoform intact. The digestion
670 reaction was stopped after 18h by 0,5M EDTA (pH 8.0) and run on a 2,5% agarose
671 (A9539-250G, Sigma-Aldrich, Darmstadt, Germany) gel for 1h at 180V. Nucleic acids
672 were visualized by adding GelRed® Nucleic Acid Gel Stain (Biotium, Solna, Sweden)
673 in a 1:10.000 dilution to the agarose gels. Agarose gels were scanned using an
674 Odyssey scanner (LI-COR Biotechnology) and bands were quantified using ImageJ.
675
676 *Stainings and immunocytochemistry*

Tissue samples were fixed in 4% paraformaldehyde for 24h and subsequently embedded in paraffin. Cells and tumor spheroids were fixed for 10 minutes in 4% paraformaldehyde and stored at 4°C until further processing. Paraffin embedded tissue samples were cut at 5µm and dried overnight. Sections were de-paraffinized and rehydrated prior to staining. Collagen was stained using the picrosirius red staining with an incubation time of 30 minutes, followed by 10 minutes washing in distilled water (81). Haematoxylin-eosin (H&E) staining was done according to standard practice (82). Images were acquired using a Nikon eclipse 90i microscope equipped with a DS-Qi1Mc camera and Nikon plan Apo objectives. NIS-Elements AR 3.2 software was used to save and export images. Quantification of collagen deposition was performed blindly with ImageJ software by conversion to binary images after color de-convolution to separate Sirius Red staining, as previously described (83).

Paraformaldehyde fixed cells and spheroids were washed with tris-buffered saline (TBS) (T5030-50TAB, Sigma-Aldrich, Darmstadt, Germany) and blocked for 30 minutes using 1% bovine serum albumin in TBS + 0,1% Tween® 20 (P7949-500ML, Sigma-Aldrich, Darmstadt, Germany). For liver tissue, antigen retrieval was done at 95°C in sodium citrate buffer or Diva Decloacker solution (DV2004, Biocare, Gothenburg, Sweden). Blocking was done using TNB blocking reagent (FP1020, Perkin-Elmer, Hägersten, Sweden) for 45 minutes and followed by an overnight incubation at 4°C with primary antibodies (supplementary table 2). A 40-minute incubation was used for the secondary antibody (Rabbit anti-mouse Alexa Fluor-488 or donkey anti-rabbit Alexa Fluor-633) and cell nuclei were stained with Hoechst for 8 minutes. Images were taken using an inverted confocal microscope (LSM 700, Zeiss,

Stockholm, Sweden) using Plan-Apochromat 20× objectives and the Zen 2009 software (Zeiss, Stockholm, Sweden). The different channels of immunofluorescent images were merged using ImageJ software. Quantifications were done blindly with ImageJ software by conversion to binary images for each channel and automated detection of staining on thresholded images using a macro.

For histological and immunohistochemical analysis of the human liver scaffolds, 4µm slides were cut from paraffin embedded blocks. The sections were de-paraffinized and rehydrated prior to staining. To retrieve the antigens, slides were microwaved at high power for 5 minutes in pre-heated 10 mM sodium citrate buffer, and subsequently left to cool down to room temperature. Following this, a single wash was performed in 100 mM Glycine in PBS, after which the slides were blocked for 2h in TNB Blocking Reagent. Slides were then incubated for 2h in the following antibodies; KI67 (1:100; SolA15, eBioscience™, Stockholm, Sweden), and EPCAM (1:100; ab71916, Abcam, Cambridge, UK). A 1h incubation was used for the secondary antibody (goat anti-rat Alexa Fluor 555 and Rabbit anti-mouse Alexa Fluor 488, ThermoFisher, Stockholm, Sweden). Sections were mounted with Fluoromount™-G (F4680-25ML, Sigma-Aldrich, Darmstadt, Germany) with DAPI (00-4959-52, Invitrogen, Stockholm, Sweden). Images were taken with using an inverted confocal microscope (LSM 780, Zeiss) using Plan-Apochromat 10× objectives and the Zen 2009 software (Zeiss).

Enzyme-Linked immune Sorbent Assay (ELISA)

Medium samples from cells and from the engrafted scaffolds were used to measure TGFβ via ELISA (88-8350-22, ThermoFisher, Stockholm, Sweden), following

manufacturer´s guidelines. The averages from 4 biological replicates and 2 technical replicates were used for calculations.

SDS-PAGE and western blot

Protein lysates in lysis buffer were mixed with 2x Laemmli buffer and heated to 95˚C for 5 minutes before being loaded onto a Precast Mini-Protean® TGX™ gels (456-9034, Biorad, Solna, Sweden). After separation, proteins were transferred to an Immobilon®-Fl membrane (IPFL0010, Millipore, Solna, Sweden) (84). The membrane was blocked using the Intercept® (TBS) blocking buffer (927-60001, Li-Cor, Bad Homburg, Germany) diluted 1:4 in PBS, and then incubated with primary and secondary antibodies. After primary and secondary antibody incubation the membrane was washed 3x15 minutes in PBS-T (PBS + 0.1% Tween®20). Primary antibodies used were BIP (ab21685, Abcam, Cambridge, UK), XBP1 (ab37152, Abcam, Cambridge, UK), p-IRE1α (PAB12435, Abnova, Heidelberg, Germany) or vinculin (14-9777-82, ThermoFisher, Stockholm, Sweden), diluted in blocking buffer with 0.1% Tween®20. Secondary antibodies used were goat-anti-rabbit Alexa 680 (A21088, Invitrogen, Stockholm, Sweden) and goat-anti-mouse IRDye 800 (Rockland, Stockholm, Sweden), diluted 1:20 000 in blocking buffer with 0.1% Tween®20 and 0.01% SDS. All incubations were carried out at room temperature for 1h or overnight at 4˚C. The membranes were scanned using an Odyssey scanner (LI-COR Biotechnology) and band intensities quantified using the Odyssey 2.1 software and normalized to the vinculin signal in each sample (84).

Gene-set enrichment analysis

Gene expression profiles of HCC with a fibrous stroma and without fibrous stroma were accessed through PubMed´s Gene Expression Omnibus via accession number GSE31370 (85). A gene-set containing 79 genes involved in the unfolded protein response was downloaded from The Harmonizome (86) and GSEA software was used to perform a gene-set enrichment assay (87).

Reactive oxygen species (ROS) assay

Generation of ROS was measured using DCFDA - Cellular ROS Detection Assay Kit (ab113851, Abcam, Cambridge, UK) in a microplate format. Cells were seeded in flat clear bottom black 96-well plates at a density of 1.0 x10^5 cells/well and left to adhere overnight. On the next day, cells were stained with 25 µM DCFDA for 45 minutes at 37°C, according to manufacturer's guidelines. After 6 hours of treatment, fluorescence was measured at 485 nm excitation and 535 nm emission wavelengths, using a Fluostar Omega plate reader. Results of the microplate assay are shown as fold change fluorescence from 6 biological replicates.

Human protein atlas

Images from biopsies from HCC patients stained with antibodies against WIPI1 (88), SHC1 (89), PPP2R5B (90) and BIP (91) were obtained through the Human Protein Atlas (92).

Statistics

Data are presented as mean ± standard error of the mean. Statistical significance was determined using an unpaired, two-tailed Student's T-test or one-way analysis of variance (ANOVA) followed by Tukey´s multiple comparison test. Survival curves

were generated with the Kaplan-Meier method and statistical comparisons were made using the log-rank method. P-values <0.05 were considered statistically significant. *In vitro* experiments were done in at least 3 biological replicates, which we define as parallel measurements of biologically distinct samples taken from independent experiments. Technical replicates we define as loading the same sample multiple times on the final assay. The *in vivo* experiments were done on at least 5 independent animals. Outliers were kept in the analyses, unless they were suspected to occur due to technical errors, in which case the experiment was repeated.

ACKNOWLEDGEMENTS

This research was funded through grants obtained from the Swedish Cancer Foundation (Cancerfonden, CAN2017/518 and CAN2013/1273), The Swedish children's cancer foundation (Barncancerfonden), the Swedish society for medical research (SSMF, S17-0092), the O.E. och Edla Johanssons stiftelse and Olga Jönssons stiftelse. These funding sources were not involved in the study design; collection, analysis and interpretation of data; writing of the report; and in the decision to submit the article for publication. We would like to thank visiting students Kim Vanhollebeke and Justine Dobbelaere for their technical assistance; GradienTech for providing us with their CellDirector assays and Paul O´Callaghan for his valuable input on our project.

Competing interest: The authors have no conflict of interest to report.

REFERENCES

1. Calderaro J, Ziol M, Paradis V, Zucman-Rossi J. Molecular and histological correlations in liver cancer. Journal of hepatology. 2019.10.1016/j.jhep.2019.06.001
2. Coulouarn C, Clement B. Stellate cells and the development of liver cancer: therapeutic potential of targeting the stroma. Journal of hepatology. 2014;60(6):1306-9.10.1016/j.jhep.2014.02.003
3. Yu G, Jing Y, Kou X, Ye F, Gao L, Fan Q, et al. Hepatic stellate cells secreted hepatocyte growth factor contributes to the chemoresistance of hepatocellular carcinoma. PloS one. 2013;8(9):e73312.10.1371/journal.pone.0073312
4. Giannelli G, Villa E, Lahn M. Transforming Growth Factor-beta as a Therapeutic Target in Hepatocellular Carcinoma. Cancer research. 2014;74(7):1890-4.10.1158/0008-5472.CAN-14-0243
5. Nitta T, Kim JS, Mohuczy D, Behrns KE. Murine cirrhosis induces hepatocyte epithelial mesenchymal transition and alterations in survival signaling pathways. Hepatology. 2008;48(3):909-19.10.1002/hep.22397
6. Dooley S, Weng H, Mertens PR. Hypotheses on the role of transforming growth factor-beta in the onset and progression of hepatocellular carcinoma. Digestive diseases. 2009;27(2):93-101.10.1159/000218340
7. Lin N, Chen Z, Lu Y, Li Y, Hu K, Xu R. Role of activated hepatic stellate cells in proliferation and metastasis of hepatocellular carcinoma. Hepatology research : the official journal of the Japan Society of Hepatology. 2014.10.1111/hepr.12356
8. Song Y, Kim SH, Kim KM, Choi EK, Kim J, Seo HR. Activated hepatic stellate cells play pivotal roles in hepatocellular carcinoma cell chemoresistance and migration in multicellular tumor spheroids. Sci Rep. 2016;6:36750.10.1038/srep36750
9. Zhang F, Hao M, Jin H, Yao Z, Lian N, Wu L, et al. Canonical hedgehog signalling regulates hepatic stellate cell-mediated angiogenesis in liver fibrosis. Br J Pharmacol. 2017;174(5):409-23.10.1111/bph.13701
10. Taura K, De Minicis S, Seki E, Hatano E, Iwaisako K, Osterreicher CH, et al. Hepatic stellate cells secrete angiopoietin 1 that induces angiogenesis in liver fibrosis. Gastroenterology. 2008;135(5):1729-38.10.1053/j.gastro.2008.07.065
11. Caja L, Dituri F, Mancarella S, Caballero-Diaz D, Moustakas A, Giannelli G, et al. TGF-beta and the Tissue Microenvironment: Relevance in Fibrosis and Cancer. Int J Mol Sci. 2018;19(5).10.3390/ijms19051294
12. Lu Y, Lin N, Chen Z, Xu R. Hypoxia-induced secretion of platelet-derived growth factor-BB by hepatocellular carcinoma cells increases activated hepatic stellate cell proliferation, migration and expression of vascular endothelial growth factor-A. Mol Med Rep. 2015;11(1):691-7.10.3892/mmr.2014.2689
13. Carloni V, Luong TV, Rombouts K. Hepatic stellate cells and extracellular matrix in hepatocellular carcinoma: more complicated than ever. Liver international : official journal of the International Association for the Study of the Liver. 2014.10.1111/liv.12465
14. Heindryckx F, Binet F, Ponticos M, Rombouts K, Lau J, Kreuger J, et al. Endoplasmic reticulum stress enhances fibrosis through IRE1alpha-mediated degradation of miR-150 and XBP-1 splicing. EMBO Mol Med. 2016;8(7):729-44.10.15252/emmm.201505925
15. Liu Z, Li C, Kang N, Malhi H, Shah VH, Maiers JL. Transforming growth factor beta (TGFbeta) cross-talk with the unfolded protein response is critical for hepatic stellate cell activation. J Biol Chem. 2019;294(9):3137-51.10.1074/jbc.RA118.005761
16. Schroder M, Kaufman RJ. ER stress and the unfolded protein response. Mutat Res-Fund Mol M. 2005;569(1-2):29-63.10.1016/j.mrfmmm.2004.06.056
17. Lam M, Marsters SA, Ashkenazi A, Walter P. Misfolded proteins bind and activate death receptor 5 to trigger apoptosis during unresolved endoplasmic reticulum stress. Elife. 2020;9.10.7554/eLife.52291

18. Acosta-Alvear D, Karagoz GE, Frohlich F, Li H, Walther TC, Walter P. The unfolded protein response and endoplasmic reticulum protein targeting machineries converge on the stress sensor IRE1. Elife. 2018;7.10.7554/eLife.43036
19. Liang H, Xiao J, Zhou Z, Wu J, Ge F, Li Z, et al. Hypoxia induces miR-153 through the IRE1alpha-XBP1 pathway to fine tune the HIF1alpha/VEGFA axis in breast cancer angiogenesis. Oncogene. 2018.10.1038/s41388-017-0089-8
20. Li XX, Zhang HS, Xu YM, Zhang RJ, Chen Y, Fan L, et al. Knockdown of IRE1alpha inhibits colonic tumorigenesis through decreasing beta-catenin and IRE1alpha targeting suppresses colon cancer cells. Oncogene. 2017;36(48):6738-46.10.1038/onc.2017.284
21. Vandewynckel YP, Laukens D, Geerts A, Bogaerts E, Paridaens A, Verhelst X, et al. The paradox of the unfolded protein response in cancer. Anticancer Res. 2013;33(11):4683-94
22. Kim H, Bhattacharya A, Qi L. Endoplasmic reticulum quality control in cancer: Friend or foe. Semin Cancer Biol. 2015;33:25-33.10.1016/j.semcancer.2015.02.003
23. Heindryckx F, Li JP. Role of proteoglycans in neuro-inflammation and central nervous system fibrosis. Matrix Biol. 2018;68-69:589-601.10.1016/j.matbio.2018.01.015
24. Bandla H, Dasgupta D, Mauer AS, Nozickova B, Kumar S, Hirsova P, et al. Deletion of endoplasmic reticulum stress-responsive co-chaperone p58(IPK) protects mice from diet-induced steatohepatitis. Hepatology research : the official journal of the Japan Society of Hepatology. 2018.10.1111/hepr.13052
25. Kwanten WJ, Vandewynckel YP, Martinet W, De Winter BY, Michielsen PP, Van Hoof VO, et al. Hepatocellular autophagy modulates the unfolded protein response and fasting-induced steatosis in mice. American journal of physiology Gastrointestinal and liver physiology. 2016;311(4):G599-G609.10.1152/ajpgi.00418.2015
26. Dasgupta D, Nakao Y, Mauer AS, Thompson JM, Sehrawat TS, Liao CY, et al. IRE1A Stimulates Hepatocyte-derived Extracellular Vesicles That Promote Inflammation in Mice With Steatohepatitis. Gastroenterology. 2020.10.1053/j.gastro.2020.06.031
27. Li J, He J, Fu Y, Hu X, Sun LQ, Huang Y, et al. Hepatitis B virus X protein inhibits apoptosis by modulating endoplasmic reticulum stress response. Oncotarget. 2017;8(56):96027-34.10.18632/oncotarget.21630
28. Sasaki M, Yoshimura-Miyakoshi M, Sato Y, Nakanuma Y. A possible involvement of endoplasmic reticulum stress in biliary epithelial autophagy and senescence in primary biliary cirrhosis. J Gastroenterol. 2015;50(9):984-95.10.1007/s00535-014-1033-0
29. Heindryckx F, Mertens K, Charette N, Vandeghinste B, Casteleyn C, Van Steenkiste C, et al. Kinetics of angiogenic changes in a new mouse model for hepatocellular carcinoma. Mol Cancer. 2010;9:219.10.1186/1476-4598-9-219
30. Hang HL, Liu XY, Wang HT, Xu N, Bian JM, Zhang JJ, et al. Hepatocyte nuclear factor 4A improves hepatic differentiation of immortalized adult human hepatocytes and improves liver function and survival. Experimental cell research. 2017;360(2):81-93.10.1016/j.yexcr.2017.08.020
31. Cormier N, Yeo A, Fiorentino E, Paxson J. Optimization of the Wound Scratch Assay to Detect Changes in Murine Mesenchymal Stromal Cell Migration After Damage by Soluble Cigarette Smoke Extract. J Vis Exp. 2015(106):e53414.10.3791/53414
32. Bise R, Kanade T, Yin Z, Huh SI. Automatic cell tracking applied to analysis of cell migration in wound healing assay. Conf Proc IEEE Eng Med Biol Soc. 2011;2011:6174-9.10.1109/IEMBS.2011.6091525
33. Oudin MJ, Weaver VM. Physical and Chemical Gradients in the Tumor Microenvironment Regulate Tumor Cell Invasion, Migration, and Metastasis. Cold Spring Harb Symp Quant Biol. 2016;81:189-205.10.1101/sqb.2016.81.030817

34. Heindryckx F, Gerwins P. Targeting the tumor stroma in hepatocellular carcinoma. World J Hepatol. 2015;7(2):165-76.10.4254/wjh.v7.i2.165
35. Koo JH, Lee HJ, Kim W, Kim SG. Endoplasmic Reticulum Stress in Hepatic Stellate Cells Promotes Liver Fibrosis via PERK-Mediated Degradation of HNRNPA1 and Up-regulation of SMAD2. Gastroenterology. 2016;150(1):181-93 e8.10.1053/j.gastro.2015.09.039
36. Hernandez-Gea V, Hilscher M, Rozenfeld R, Lim MP, Nieto N, Werner S, et al. Endoplasmic reticulum stress induces fibrogenic activity in hepatic stellate cells through autophagy. Journal of hepatology. 2013;59(1):98-104.10.1016/j.jhep.2013.02.016
37. Kim RS, Hasegawa D, Goossens N, Tsuchida T, Athwal V, Sun X, et al. The XBP1 Arm of the Unfolded Protein Response Induces Fibrogenic Activity in Hepatic Stellate Cells Through Autophagy. Sci Rep. 2016;6:39342.10.1038/srep39342
38. Mao YQ, Fan XM. Autophagy: A new therapeutic target for liver fibrosis. World J Hepatol. 2015;7(16):1982-6.10.4254/wjh.v7.i16.1982
39. Zeng L, Zampetaki A, Margariti A, Pepe AE, Alam S, Martin D, et al. Sustained activation of XBP1 splicing leads to endothelial apoptosis and atherosclerosis development in response to disturbed flow. Proc Natl Acad Sci U S A. 2009;106(20):8326-31.10.1073/pnas.0903197106
40. Yoshida H, Matsui T, Yamamoto A, Okada T, Mori K. XBP1 mRNA is induced by ATF6 and spliced by IRE1 in response to ER stress to produce a highly active transcription factor. Cell. 2001;107(7):881-91.10.1016/s0092-8674(01)00611-0
41. Cassimeris L, Engiles JB, Galantino-Homer H. Detection of endoplasmic reticulum stress and the unfolded protein response in naturally-occurring endocrinopathic equine laminitis. BMC Vet Res. 2019;15(1):24.10.1186/s12917-018-1748-x
42. Kishino A, Hayashi K, Hidai C, Masuda T, Nomura Y, Oshima T. XBP1-FoxO1 interaction regulates ER stress-induced autophagy in auditory cells. Sci Rep. 2017;7(1):4442.10.1038/s41598-017-02960-1
43. Yoshida H, Oku M, Suzuki M, Mori K. pXBP1(U) encoded in XBP1 pre-mRNA negatively regulates unfolded protein response activator pXBP1(S) in mammalian ER stress response. J Cell Biol. 2006;172(4):565-75.10.1083/jcb.200508145
44. Park MH, Kim AK, Manandhar S, Oh SY, Jang GH, Kang L, et al. CCN1 interlinks integrin and hippo pathway to autoregulate tip cell activity. Elife. 2019;8.10.7554/eLife.46012
45. Borkham-Kamphorst E, Steffen BT, Van de Leur E, Tihaa L, Haas U, Woitok MM, et al. Adenoviral CCN gene transfers induce in vitro and in vivo endoplasmic reticulum stress and unfolded protein response. Biochim Biophys Acta. 2016;1863(11):2604-12.10.1016/j.bbamcr.2016.07.006
46. Borkham-Kamphorst E, Steffen BT, van de Leur E, Haas U, Weiskirchen R. Portal myofibroblasts are sensitive to CCN-mediated endoplasmic reticulum stress-related apoptosis with potential to attenuate biliary fibrogenesis. Cell Signal. 2018;51:72-85.10.1016/j.cellsig.2018.07.005
47. Amann T, Bataille F, Spruss T, Muhlbauer M, Gabele E, Scholmerich J, et al. Activated hepatic stellate cells promote tumorigenicity of hepatocellular carcinoma. Cancer Sci. 2009;100(4):646-53.10.1111/j.1349-7006.2009.01087.x
48. Han W, Chen S, Yuan W, Fan Q, Tian J, Wang X, et al. Oriented collagen fibers direct tumor cell intravasation. Proceedings of the National Academy of Sciences of the United States of America. 2016;113(40):11208-13.10.1073/pnas.1610347113
49. Kumar S, Das A, Sen S. Extracellular matrix density promotes EMT by weakening cell-cell adhesions. Mol Biosyst. 2014;10(4):838-50.10.1039/c3mb70431a

50. Liu WT, Jing YY, Yu GF, Chen H, Han ZP, Yu DD, et al. Hepatic stellate cell promoted hepatoma cell invasion via the HGF/c-Met signaling pathway regulated by p53. Cell Cycle. 2016;15(7):886-94.10.1080/15384101.2016.1152428
51. Shuda M, Kondoh N, Imazeki N, Tanaka K, Okada T, Mori K, et al. Activation of the ATF6, XBP1 and grp78 genes in human hepatocellular carcinoma: a possible involvement of the ER stress pathway in hepatocarcinogenesis. Journal of hepatology. 2003;38(5):605-14
52. Corazzari M, Gagliardi M, Fimia GM, Piacentini M. Endoplasmic Reticulum Stress, Unfolded Protein Response, and Cancer Cell Fate. Front Oncol. 2017;7:78.10.3389/fonc.2017.00078
53. Wu Y, Shan B, Dai J, Xia Z, Cai J, Chen T, et al. Dual Role for Inositol-requiring Enzyme 1alpha in Promoting the Development of Hepatocellular Carcinoma during Diet-induced Obesity. Hepatology. 2018.10.1002/hep.29871
54. Ghosh R, Wang L, Wang ES, Perera BG, Igbaria A, Morita S, et al. Allosteric inhibition of the IRE1alpha RNase preserves cell viability and function during endoplasmic reticulum stress. Cell. 2014;158(3):534-48.10.1016/j.cell.2014.07.002
55. Cubillos-Ruiz JR, Bettigole SE, Glimcher LH. Tumorigenic and Immunosuppressive Effects of Endoplasmic Reticulum Stress in Cancer. Cell. 2017;168(4):692-706.10.1016/j.cell.2016.12.004
56. Li X, Zhu H, Huang H, Jiang R, Zhao W, Liu Y, et al. Study on the effect of IRE1a on cell growth and apoptosis via modulation PLK1 in ER stress response. Molecular and cellular biochemistry. 2012;365(1-2):99-108.10.1007/s11010-012-1248-4
57. Pellegrino R, Calvisi DF, Ladu S, Ehemann V, Staniscia T, Evert M, et al. Oncogenic and tumor suppressive roles of polo-like kinases in human hepatocellular carcinoma. Hepatology. 2010;51(3):857-68.10.1002/hep.23467
58. Auf G, Jabouille A, Guerit S, Pineau R, Delugin M, Bouchecareilh M, et al. Inositol-requiring enzyme 1alpha is a key regulator of angiogenesis and invasion in malignant glioma. Proceedings of the National Academy of Sciences of the United States of America. 2010;107(35):15553-8.10.1073/pnas.0914072107
59. Abuaita BH, Burkholder KM, Boles BR, O'Riordan MX. The Endoplasmic Reticulum Stress Sensor Inositol-Requiring Enzyme 1alpha Augments Bacterial Killing through Sustained Oxidant Production. mBio. 2015;6(4):e00705.10.1128/mBio.00705-15
60. Chan SMH, Lowe MP, Bernard A, Miller AA, Herbert TP. The inositol-requiring enzyme 1 (IRE1alpha) RNAse inhibitor, 4micro8C, is also a potent cellular antioxidant. Biochem J. 2018;475(5):923-9.10.1042/BCJ20170678
61. Riaz TA, Junjappa RP, Handigund M, Ferdous J, Kim HR, Chae HJ. Role of Endoplasmic Reticulum Stress Sensor IRE1alpha in Cellular Physiology, Calcium, ROS Signaling, and Metaflammation. Cells. 2020;9(5).10.3390/cells9051160
62. Zeeshan HM, Lee GH, Kim HR, Chae HJ. Endoplasmic Reticulum Stress and Associated ROS. Int J Mol Sci. 2016;17(3):327.10.3390/ijms17030327
63. Dubbelboer IR, Pavlovic N, Heindryckx F, Sjogren E, Lennernas H. Liver Cancer Cell Lines Treated with Doxorubicin under Normoxia and Hypoxia: Cell Viability and Oncologic Protein Profile. Cancers (Basel). 2019;11(7).10.3390/cancers11071024
64. Montiel-Duarte C, Ansorena E, Lopez-Zabalza MJ, Cenarruzabeitia E, Iraburu MJ. Role of reactive oxygen species, glutathione and NF-kappaB in apoptosis induced by 3,4-methylenedioxymethamphetamine ("Ecstasy") on hepatic stellate cells. Biochem Pharmacol. 2004;67(6):1025-33.10.1016/j.bcp.2003.10.020
65. Kong M, Chen X, Lv F, Ren H, Fan Z, Qin H, et al. Serum response factor (SRF) promotes ROS generation and hepatic stellate cell activation by epigenetically stimulating NCF1/2 transcription. Redox Biol. 2019;26:101302.10.1016/j.redox.2019.101302

66. Takaki A, Yamamoto K. Control of oxidative stress in hepatocellular carcinoma: Helpful or harmful? World J Hepatol. 2015;7(7):968-79.10.4254/wjh.v7.i7.968
67. Uchida D, Takaki A, Oyama A, Adachi T, Wada N, Onishi H, et al. Oxidative Stress Management in Chronic Liver Diseases and Hepatocellular Carcinoma. Nutrients. 2020;12(6).10.3390/nu12061576
68. Tien Kuo M, Savaraj N. Roles of reactive oxygen species in hepatocarcinogenesis and drug resistance gene expression in liver cancers. Mol Carcinog. 2006;45(9):701-9.10.1002/mc.20240
69. Klieser E, Mayr C, Kiesslich T, Wissniowski T, Fazio PD, Neureiter D, et al. The Crosstalk of miRNA and Oxidative Stress in the Liver: From Physiology to Pathology and Clinical Implications. Int J Mol Sci. 2019;20(21).10.3390/ijms20215266
70. Heindryckx F, Bogaerts E, Coulon SH, Devlies H, Geerts AM, Libbrecht L, et al. Inhibition of the placental growth factor decreases burden of cholangiocarcinoma and hepatocellular carcinoma in a transgenic mouse model. Eur J Gastroenterol Hepatol. 2012;24(9):1020-32.10.1097/MEG.0b013e3283554219
71. Calitz C, Pavlović N, Rosenquist J, Zagami C, Samanta A, Heindryckx F. A Biomimetic Model for Liver Cancer to Study Tumor-Stroma Interactions in a 3D Environment with Tunable Bio-Physical Properties. JoVE. 2020(162):e61606.doi:10.3791/61606
72. Calitz C, Hamman JH, Fey SJ, Viljoen AM, Gouws C, Wrzesinski K. A sub-chronic Xysmalobium undulatum hepatotoxicity investigation in HepG2/C3A spheroid cultures compared to an in vivo model. J Ethnopharmacol. 2019;239:111897.10.1016/j.jep.2019.111897
73. Fuchs PO, Calitz C, Pavlovic N, Binet F, Solbak SMO, Danielson UH, et al. Fibrin fragment E potentiates TGF-beta-induced myofibroblast activation and recruitment. Cell Signal. 2020;72:109661.10.1016/j.cellsig.2020.109661
74. Krauthamer M, Rouvinov K, Ariad S, Man S, Walfish S, Pinsk I, et al. A study of inflammation-based predictors of tumor response to neoadjuvant chemoradiotherapy for locally advanced rectal cancer. Oncology. 2013;85(1):27-32.10.1159/000348385
75. Heindryckx F. 2020 [https://doi.org/10.5061/dryad.6wwpzgmv2
76. Capes-Davis A, Theodosopoulos G, Atkin I, Drexler HG, Kohara A, MacLeod RA, et al. Check your cultures! A list of cross-contaminated or misidentified cell lines. Int J Cancer. 2010;127(1):1-8.10.1002/ijc.25242
77. Mazza G, Al-Akkad W, Telese A, Longato L, Urbani L, Robinson B, et al. Rapid production of human liver scaffolds for functional tissue engineering by high shear stress oscillation-decellularization. Sci Rep. 2017;7(1):5534.10.1038/s41598-017-05134-1
78. Thanapirom K, Frenguelli L, Al-Akkad W, Zhang ZZ, Pinzani M, Mazza G, et al. Optimization and validation of a novel three-dimensional co-culture system in decellularized human liver scaffold for the study of liver fibrosis and cancer. Journal of hepatology. 2019;70:E24-E.Doi 10.1016/S0618-8278(19)30042-8
79. Prabst K, Engelhardt H, Ringgeler S, Hubner H. Basic Colorimetric Proliferation Assays: MTT, WST, and Resazurin. Methods Mol Biol. 2017;1601:1-17.10.1007/978-1-4939-6960-9_1
80. Pinto BI, Cruz ND, Lujan OR, Propper CR, Kellar RS. In Vitro Scratch Assay to Demonstrate Effects of Arsenic on Skin Cell Migration. J Vis Exp. 2019(144).10.3791/58838
81. Huang Y, de Boer WB, Adams LA, MacQuillan G, Rossi E, Rigby P, et al. Image analysis of liver collagen using sirius red is more accurate and correlates better with serum fibrosis markers than trichrome. Liver Int. 2013;33(8):1249-56.10.1111/liv.12184
82. Cardiff RD, Miller CH, Munn RJ. Manual hematoxylin and eosin staining of mouse tissue sections. Cold Spring Harb Protoc. 2014;2014(6):655-8.10.1101/pdb.prot073411

83. Ruifrok AC, Johnston DA. Quantification of histochemical staining by color deconvolution. Analytical and quantitative cytology and histology / the International Academy of Cytology [and] American Society of Cytology. 2001;23(4):291-9
84. Eaton SL, Hurtado ML, Oldknow KJ, Graham LC, Marchant TW, Gillingwater TH, et al. A guide to modern quantitative fluorescent western blotting with troubleshooting strategies. J Vis Exp. 2014(93):e52099.10.3791/52099
85. Seok JY, Na DC, Woo HG, Roncalli M, Kwon SM, Yoo JE, et al. A fibrous stromal component in hepatocellular carcinoma reveals a cholangiocarcinoma-like gene expression trait and epithelial-mesenchymal transition. Hepatology. 2012;55(6):1776-86.10.1002/hep.25570
86. Rouillard AD, Gundersen GW, Fernandez NF, Wang Z, Monteiro CD, McDermott MG, et al. The harmonizome: a collection of processed datasets gathered to serve and mine knowledge about genes and proteins. Database (Oxford). 2016;2016.10.1093/database/baw100
87. Subramanian A, Tamayo P, Mootha VK, Mukherjee S, Ebert BL, Gillette MA, et al. Gene set enrichment analysis: a knowledge-based approach for interpreting genome-wide expression profiles. Proc Natl Acad Sci U S A. 2005;102(43):15545-50.10.1073/pnas.0506580102
88. https://www.proteinatlas.org/ENSG00000070540-WIPI1/pathology/liver+cancer.doi: . The Human Protein Atlas. 2019;V19
89. https://www.proteinatlas.org/ENSG00000160691-SHC1/pathology/liver+cancer. The Human Protein Atlas.V19
90. https://www.proteinatlas.org/ENSG00000068971-PPP2R5B/pathology/liver+cancer#imid_9419368. The Human Protein Atlas.V19
91. https://www.proteinatlas.org/ENSG00000044574-HSPA5/pathology/liver+cancer. The Human Protein Atlas.V19
92. Uhlen M, Fagerberg L, Hallstrom BM, Lindskog C, Oksvold P, Mardinoglu A, et al. Proteomics. Tissue-based map of the human proteome. Science. 2015;347(6220):1260419.10.1126/science.1260419

Figures

Fig. 1. Inhibiting IRE1α reduces tumor burden *in vivo*. *(A)* Representative images of liver slides stained with hematoxylin and eosin (H&E), Sirius red and αSMA-antibodies. ***(B)*** tumor burden of mice with DEN-induced HCC treated with 4μ8C or vehicle-treated controls. ***(C)*** Quantification of percentage of collagen and ***(D)*** αSMA on liver slides. ***(E)*** mRNA expression of *Pcna* in liver tissue from mice with HCC treated with 4μ8C ***(F).*** Heatmap showing protein expression levels in healthy liver, DEN-induced HCC and DEN-induced HCC treated with 4μ8C from 3 biological replicates per group. P-values were calculated via the Student´s T-test, scale bars = 120μm.

Fig. 2. Increased expression of ER-stress markers in mice with HCC. *(A)* mRNA expression of ER-stress markers *Edem1, Ero1b, Grp94, Herp, Atf4, Eif2ak3, Ddit3* and *Hspa5* in liver tissue from healthy mice; and tumor tissue and surrounding non-tumoral tissue from mice with DEN-induced HCC. ***(B)*** *Hspa5*-mRNA and ***(C)*** protein expression of BIP in murine liver tissue. ***(D)*** Ratio of spliced to unspliced *XBP1* in liver tissue from healthy mice; and tumor tissue and surrounding non-tumoral tissue from mice with DEN-induced HCC, treated with 4μ8C. ***(E)*** Representative western blot image of spliced and unspliced XBP1 protein and vinculin in healthy liver, DEN-induced HCC and DEN-induced HCC treated with 4μ8C. **(F)** quantification of spliced and unspliced XBP1, normalized to total vinculin levels. ***(G)*** Ratio of spliced to unspliced XBP1 protein levels. ***(H)*** Representative images and **(I)** quantification of liver tissue sections stained with antibodies against spliced XBP1. P-values were calculated via the Student´s T-test with 5 biological replicates per group. Scale bars = 120μm.

Fig 3 Activation of the unfolded protein response pathway is increased in patients with fibrotic HCC. *(A)* Heat map showing gene-set enrichment analysis results from samples from fibrous HCC versus non-fibrous HCC. ***(C)*** Immunohistochemically stained liver biopsies from HCC-patients obtained from the human protein atlas, using antibodies against IRE1α-mediated actors of the unfolded protein response: WIPI1, SHC1, PPP2R5B and BIP. ***(D)*** Kaplan-Meier survival curves of

HCC-patients with high or low expression of *WIPI1, SHC1, PPP2R5B* and *BIP*. P-values were calculated *via* a Log-Rank test.

Fig. 4. Tumor cells secrete factors that induce ER-stress in stellate cells, which contributes to their activation. ***(A)*** mRNA-expression of ER-stress markers *ATF6, ATF4, EIF2AK3, GADD34, EDEM1, DDIT3* and *HSPA5*, in stellate cells (LX2) co-cultured with cancer cells (HepG2 or Huh7) and treated with 4μ8C or control. **(B)** Detection of spliced (*XBP1s*) and unspliced *XBP1* (*XBP1u*) *via* qPCR and ***(C)*** *via* digestion of the XBP1u-RT-qPCR product by *Pst-I* and subsequent visualization by separation of on agarose gel. ***(D)*** Quantified ratio of spliced and unspliced measured on agarose gel after digestion by *Pst-I* (***E)*** protein expression of p-IRE1α and vinculin in stellate cells (LX2) co-cultured with cancer cells (HepG2 or Huh7) in transwell assays and treated with 4μ8C or control. (***F)*** mRNA-expression of stellate cell activation markers *ACTA2* and (***G)*** collagen in LX2-cells co-cultured with HepG2 or Huh7-cells and treated with or without 4μ8C. P-values were calculated via ANOVA with 10 biological replicates per group.

Fig. 5. Inhibiting IRE1α decreases stellate cell activation in human liver 3D scaffolds engrafted with stellate cells and tumor cells. ***(A)*** Representative images of H&E and Sirius red stained slides of decellularized human liver scaffolds engrafted with LX2 stellate cells and HepG2-tumor cells treated with 4μ8C or control. ***(B)*** quantification of collagen stained area fraction of liver scaffolds engrafted with LX2 stellate cells and HepG2-tumor cells treated with 4μ8C or control. ***(C)*** mRNA-expression of the stellate cells activation marker collagen and ER-stress markers *HSPA5*, spliced *XBP-1* (XBP1-S) and *DDIT3* in liver scaffolds engrafted with stellate cells (LX2) and cancer cells (HepG2), treated with 4μ8C or control. P-values were calculated via ANOVA from 3 biological replicates per group, scale bars = 100μm.

Fig. 6. Inhibition of IRE1α decreases tumor cell proliferation. ***(A)*** *PCNA* mRNA-expression of HepG2 or Huh7-cells grown with LX2-cells in transwell inserts and treated with the IRE1α-inhibitor 4μ8C or control. ***(B)*** Relative cell number of LX2 and HepG2 or ***(C)*** LX2 and Huh7-cells treated with 4μ8C or control. ***(D)*** Representative images of tumor cells (HepG2 or Huh7) and LX2-stellate cells

stained with antibodies against the HCC-marker EPCAM and the proliferation marker KI67. ***(E)*** Cell proliferation of HepG2 or HepG2+LX2 spheroids and ***(F)*** Huh7 or Huh7+LX2 spheroids treated with 4μ8C or control. P-values were calculated via the Student´s T-test from 9 biological replicates per group, scale bars = 50μm.

Fig. 7. Inhibition of IRE1α decreases cell proliferation and improves liver function in human liver scaffolds engrafted with stellate cells and tumor cells. ***(A)*** *PCNA* and ***(B)*** *HNF4A* expression of human liver scaffolds engrafted with HepG2-tumor cells and LX2-stellate cells, treated with 4μ8C or control. ***(C)*** Representative images of tumor cells (HepG2) and LX2-stellate cells stained with antibodies against the HCC-marker EPCAM and the proliferation marker KI67. P-values were calculated via ANOVA on 3 biological replicates per group, scale bars = 100μm.

Fig. 8. Inhibition of IRE1α decreases cell migration. ***(A)*** mRNA-expression of pro-metastatic markers MMP9 and ***(B)*** MMP1 in HepG2 and Huh7-cells co-cultured with LX2-cells and treated with 4μ8C or control. ***(C)*** Scratch wound on HepG2-cells and LX2-cells treated with 4μ8C or control. ***(D)*** Images of Cell Tracker stained HepG2-cells (Green) and LX2-cells (Red) invading the scratch area. ***(E)*** Quantification of wound size in HepG2-cells and LX2-cells treated with 4μ8C or control. ***(F)*** Number of HepG2-cells and LX2-cells invading the scratch wound after 24h in co-cultures and ***(G)*** mono-cultures. P-values were calculated via the Student´s T-test from 10 biological replicates per group (panel A and B) or 6 biological replicates per group (panel E-G), scale bars = 120μm.

Fig. 9. Silencing IRE1α in LX2-cells mimics 4μ8C. ***(A)*** *ERN1*-mRNA-expression of LX2-cells transfected with IRE1α-siRNA (si-IRE1α) or mock-transfected (Scr) ***(B)*** PCNA-mRNA-expression of HepG2-cells co-cultured with IRE1α-silenced LX2-cells or controls ***(C).*** Relative cell numbers in co-cultures of HepG2-cells and IRE1α-silenced LX2-cells or controls. ***(D)*** *ERN1*-mRNA-expression of HepG2- and Huh7-cells transfected with IRE1α-siRNA (si-IRE1α) or mock-transfected (Scr). (***E)*** Relative cell numbers in co-cultures LX2-cells or and si-RNE. Transfected HepG2 or Huh7 cells or mock-transfected controls (Scr). P-values were calculated via the Student´s T-test from 3 biological replicates per group (panel A, B and D) or 6 biological replicates (panel C and E).

Fig. 10: Inhibiting IRE1α alters generation of ROS. ***(A)*** intracellular ROS-levels in LX2, HepG2 and Huh7 cells treated with *50* µM 4µ8C, 100 µM 4µ8C or controls. ***(B)*** intracellular ROS-levels in LX2, HepG2 and Huh7 cells transfected with IRE1α-siRNA (si-IRE1α) or mock-transfected (Scr). P-values were calculated via the Student´s T-test from 3 biological replicates per group

Figure 2 – Figure supplement 1. Activation of the unfolded protein response is mainly located in the stroma of mice with HCC. Liver tissue from mice with DEN-induced HCC, stained with αSMA-antibodies and co-stained with antibodies against (**A)** spliced XBP1, ***(B)*** total XBP1, ***(C)*** IRE1α ***(D)*** phopho-IRE1α and ***(E)*** BIP. scale bars = 50µm.

Figure 2 – Figure supplement 2. Expression of ER-stress markers is localized in close vicinity to αSMA. Immunofluorescent images from tissue from mice with DEN-induced HCC, stained with αSMA-antibodies and co-stained with antibodies against (**A)** spliced XBP1, ***(B)*** total XBP1, ***(C)*** IRE1α ***(D)*** phopho-IRE1α and ***(E)*** BIP. (**F)** immunofluorescent image from DEN-induced HCC stained with antibodies against spliced XBP1.

Figure 4 – Figure supplement 1. Secretion of TGFβ by tumor cells activates stellate cells and induces ER-stress. ***(A)*** concentration of TGFβ in medium from tumor cells (HepG2 or Huh7) grown in mono-culture or co-cultured with LX2-stellate cells, treated with 4µ8C or control. ***(B)*** concentration of TGFβ in medium from liver scaffolds engrafted with stellate cells ***(C)*** (LX2) and tumor cells (HepG2) treated with 4µ8C or control. mRNA-expression of the ER-stress markers *DDIT3*, ***(D)*** spliced XBP1, ***(E)*** unspliced XBP1 and ***(F)*** *HSPA5* in hepatic stellate cells (LX2) grown as mono-culture or in co-cultures with the cancer cell lines HepG2 and Huh7 treated with the TGFβ receptor inhibitor SB-431541 or control**.** (***G)*** mRNA-expression of stellate cell activation markers *ACTA2* and (***H)*** collagen in LX2-cells grown with HepG2 or Huh7-cells and treated with SB-431541 or control. P-values were calculated via the Student´s T-test from 7 biological replicates per group.

Figure 8 – Figure supplement 1. Inhibiting IRE1α decreases chemotaxis. ***(A)*** migration plots of LX2-cells co-cultured with HepG2-cells exposed to an FBS-gradient (increasing towards the right) and treated with control or ***(B)*** 4μ8C ***(C)*** Quantification of total migration and ***(D)*** directional migration of LX2-cells (co-cultured with HepG2-cells) towards an FBS-gradient with or without 4μ8C. ***(E)*** Migration plots of HepG2-cells co-cultured with LX2-stellate cells and exposed to an FBS-gradient and treated with control or ***(F)*** 4μ8C. ***(G)*** Quantification of total migration and ***(H)*** directional migration of HepG2-cells (co-cultured with LX2-cells) towards an FBS-gradient with or without 4μ8C. P-values were calculated via the Student´s T-test from 3 biological replicates per group. Red lines indicate migration towards the gradient, while black lines indicate migration away from the gradient.

Figure 9 – Figure supplement 1 ***(A)*** Proliferation of spheroids of HepG2-cells and IRE1α-silenced LX2-cells or controls ***(B)*** Images and ***(C)*** quantification of αSMA-stained spheroids with HepG2-cells and IRE1α-silenced LX2-cells or controls. ***(D)*** Images and ***(E)*** quantification of scratch wound of HepG2-cells co-cultured with IRE1α-silenced LX2-cells or controls. P-values were calculated via the Student´s T-test from 3 biological replicates per group, Scale bars = 50μm (E) or 120μm (G).

Supplementary table 1. Table with primer sequences

Supplementary table 2: table with antibodies used for staining

Table 1: A proteomics array using the Olink Mouse Exploratory assay – source data figure 1F

		CTL		Den		DEN+4u8c		Statistical significance		
PROTEIN NAME	**Biological process**	**mean**	**St. Dev**	**Average**	**St. Dev**	**Average**	**St. Dev**	**DEN vs Ctrl**	**DEN vs 4u8C**	**Ctrl vs 4u8c**
CLMP	Not prognostic in HCC	1,68	0,14	2,97	1,00	2,48	0,64	*		

YES1	HCC promotor	7,11	0,29	7,51	0,20	7,44	0,19	*		
FOXO1	Tumor suppressor	4,15	0,06	4,12	0,73	3,87	0,49			
PLA2G4A	HCC promotor	3,42	0,38	5,70	1,36	5,04	0,80	*		*
PRDX5	HCC promotor	7,37	0,49	7,23	0,26	6,67	0,34		*	
TGFA	Tumor growth factor	5,36	0,52	6,81	0,64	6,93	0,88	*		*
EPO	Unfavorable prognotic marker	3,20	0,34	3,71	0,35	3,37	0,33			
AXIN1	HCC promotor	4,24	0,38	4,80	0,37	4,39	0,35			
FST	HCC promotor	5,87	0,31	8,04	0,73	7,50	0,71	*		*
NADK	Not prognostic in HCC	10,10	0,13	10,14	0,18	10,30	0,27			
SNAP29	Not prognostic in HCC	7,70	0,32	7,87	0,32	7,62	0,30			
S100A4	HCC promotor	2,73	0,74	7,01	0,62	6,85	0,97	*		*
KITLG	Metastasis	2,48	0,42	3,74	0,62	3,31	0,98	*		
GFRA1	HCC promotor	4,40	0,35	5,07	0,40	4,92	0,39	*		
PPP1R2	Not prognostic in HCC	4,37	0,16	4,86	0,46	4,47	0,43			
CYR61	HCC promotor	2,40	0,53	4,14	1,64	3,13	1,22	*		
AHR	Not prognostic in HCC	6,95	0,46	7,68	0,74	7,38	0,64			
CCL2	HCC promotor	4,59	0,58	9,69	2,04	8,93	1,56	*		*
QDPR	Not prognostic in HCC	7,71	0,11	7,72	0,14	7,54	0,15			
FAS	HCC promotor	8,66	0,18	8,83	0,18	8,70	0,18			
RIOX2	HCC promotor	7,10	0,15	7,71	0,38	7,59	0,14	*		*
EPCAM	HCC promotor	1,56	0,33	3,16	1,14	3,27	0,89	*		
CCL3	Prognostic marker	1,49	0,39	4,42	1,86	3,73	1,07	*		*
CRIM1	HCC promotor	2,46	0,28	3,71	1,09	3,21	0,56	*		*
HGF	Tumor growth factor	6,69	0,35	7,94	1,01	7,41	0,71	*		
SEZ6L2	HCC promotor	-0,29	0,15	0,61	0,53	0,19	0,29	*		
IL1A	Inflammation and fibrosis	6,65	0,51	8,35	0,65	7,62	0,54	*		*
DDAH1	HCC promotor	8,04	0,22	8,18	0,05	7,84	0,18		*	

ACVRL1	Not prognostic in HCC	2,09	0,18	3,44	1,31	2,81	0,47			
CXCL9	Inflammation and fibrosis	3,68	0,86	7,71	1,68	6,65	1,58	*		*
MAP2K6	Not prognostic in HCC	7,75	0,15	7,98	0,41	7,88	0,28			
CASP3	Tumor surrpressor	9,22	0,19	9,74	0,35	9,43	0,26			
PDGFB	Tumor growth factor	3,52	0,31	4,96	1,27	3,97	0,40	*		
IGSF3	Unfavorable prognotic marker	3,12	0,28	4,19	0,82	3,64	0,72			
CXCL1	HCC promotor	3,77	0,40	5,74	0,78	5,06	0,51	*		*
PAK4	HCC promotor	3,47	0,42	4,39	0,68	3,93	0,54			
LPL	Not prognostic in HCC	1,66	0,40	2,44	0,45	2,02	0,60			
DCTN2	Unfavorable prognotic marker	5,48	1,31	5,67	0,70	4,98	0,55			
NTF3	Not prognostic in HCC	2,16	0,27	2,80	0,71	2,27	0,40			
TNFSF12	HCC promotor	5,28	0,35	6,00	0,76	5,59	0,62			
CCL20	Unfavorable prognotic marker	5,20	0,34	5,92	0,81	5,53	0,66			
FLI1	HCC promotor	1,91	0,22	3,73	1,38	2,98	0,83			
TPP1	Unfavorable prognotic marker	3,67	0,38	4,24	0,64	3,73	0,50			
PARP1	Unfavorable prognotic marker	10,30	0,72	10,93	0,49	10,51	0,62			

Table 2: Genes the contributed to the core-enrichment of the GSEA

Probe	Description	Rank Gene list	Rank Metric score	Core enrichment	UPR branch
ASNS	asparagine synthetase (glutamine-hydrolyzing) [Source:HGNC Symbol;Acc:HGNC:753]	207	0.940	Yes	Perk

PPP2R5B	protein phosphatase 2 regulatory subunit B'beta [Source:HGNC Symbol;Acc:HGNC:9310]	423	0.821	Yes	Ire1a
CCL2	C-C motif chemokine ligand 2 [Source:HGNC Symbol;Acc:HGNC:10618]	847	0.689	Yes	Ire1a and Perk
EXOSC9	exosome component 9 [Source:HGNC Symbol;Acc:HGNC:9137]	1004	0.654	Yes	Ire1a and Perk
WIPI1	WD repeat domain, phosphoinositide interacting 1 [Source:HGNC Symbol;Acc:HGNC:25471]	1022	0.649	Yes	Ire1a
KDELR3	KDEL endoplasmic reticulum protein retention receptor 3 [Source:HGNC Symbol;Acc:HGNC:6306]	1106	0.635	Yes	Ire1a
SHC1	SHC adaptor protein 1 [Source:HGNC Symbol;Acc:HGNC:10840]	2691	0.432	Yes	Ire1a
TPP1	tripeptidyl peptidase 1 [Source:HGNC Symbol;Acc:HGNC:2073]	2884	0.414	Yes	Ire1a
HDGF	heparin binding growth factor [Source:HGNC Symbol;Acc:HGNC:4856]	3235	0.386	Yes	Ire1a
TLN1	talin 1 [Source:HGNC Symbol;Acc:HGNC:11845]	3264	0.384	Yes	Ire1a
EXTL3	exostosin like glycosyltransferase 3 [Source:HGNC Symbol;Acc:HGNC:3518]	3488	0.365	Yes	Ire1a
TSPYL2	TSPY like 2 [Source:HGNC Symbol;Acc:HGNC:24358]	3680	0.350	Yes	Ire1a
MBTPS1	membrane bound transcription factor peptidase, site 1 [Source:HGNC Symbol;Acc:HGNC:15456]	3996	0.327	Yes	Atf6
PDIA5	protein disulfide isomerase family A member 5 [Source:HGNC Symbol;Acc:HGNC:24811]	4530	0.294	Yes	Ire1a
DCTN1	dynactin subunit 1 [Source:HGNC Symbol;Acc:HGNC:2711]	4638	0.287	Yes	Ire1a
DNAJC3	DnaJ heat shock protein family (Hsp40) member C3 [Source:HGNC Symbol;Acc:HGNC:9439]	4761	0.281	Yes	Ire1a
SULT1A4	sulfotransferase family 1A member 4 [Source:HGNC Symbol;Acc:HGNC:30004]	4938	0.272	Yes	Ire1a
PARN	poly(A)-specific ribonuclease [Source:HGNC Symbol;Acc:HGNC:8609]	5037	0.266	Yes	Perk
ADD1	adducin 1 [Source:HGNC Symbol;Acc:HGNC:243]	5375	0.250	Yes	Ire1a
ERN1	endoplasmic reticulum to nucleus signaling 1 [Source:HGNC Symbol;Acc:HGNC:3449]	5411	0.248	Yes	Ire1a

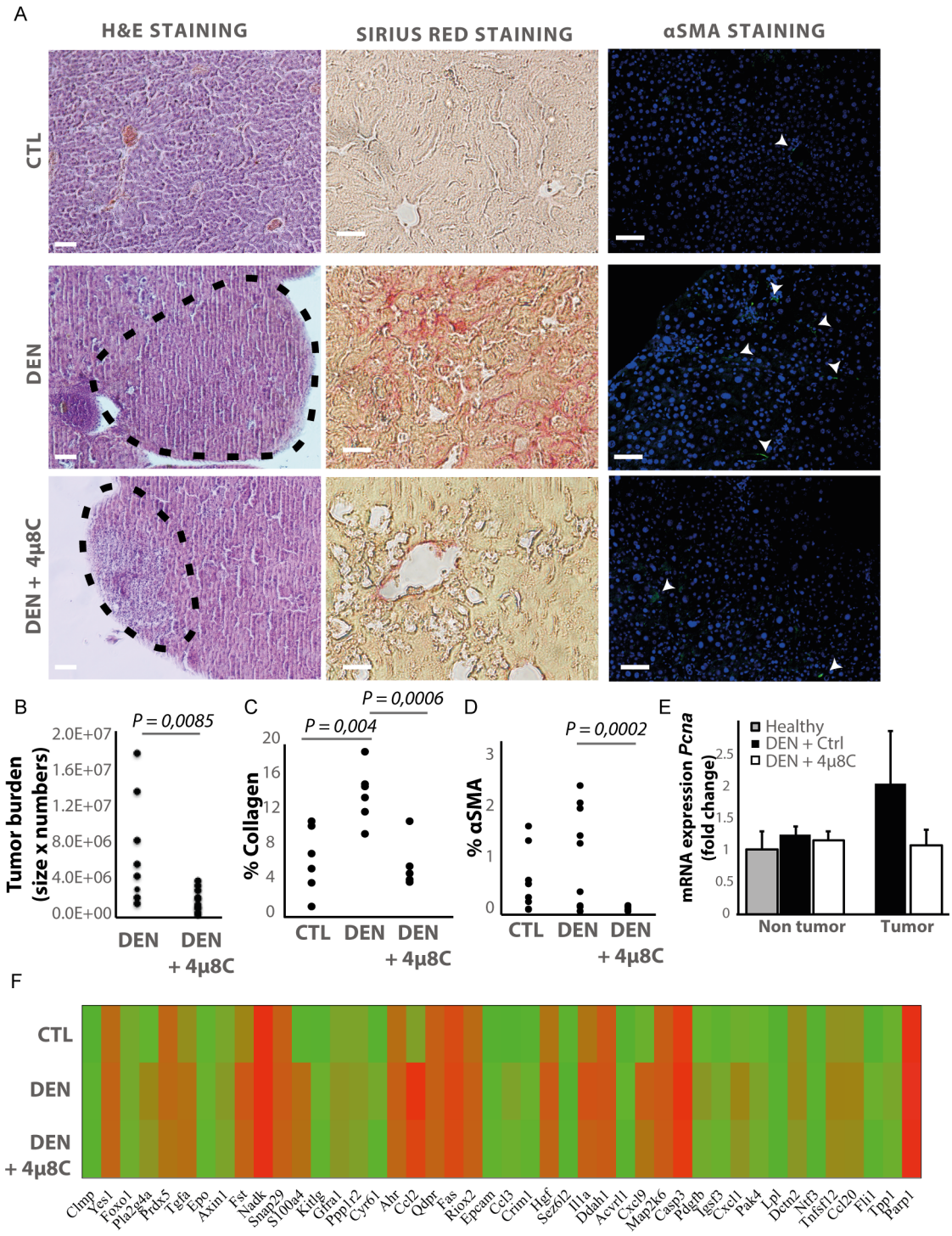
A
H&E STAINING
SIRIUS RED STAINING
αSMA STAINING
CTL
DEN
DEN + 4μ8C
B
Tumor burden (size x numbers)
P = 0,0085
2.0E+07
1.6E+07
1.2E+07
8.0E+06
4.0E+06
0.0E+00
DEN
DEN + 4μ8C
C
% Collagen
P = 0,004
P = 0,0006
20
16
12
8
4
0
CTL
DEN
DEN + 4μ8C
D
% αSMA
P = 0,0002
3
2
1
0
CTL
DEN
DEN + 4μ8C
E
mRNA expression Pcna (fold change)
Healthy
DEN + Ctrl
DEN + 4μ8C
2.5
2
1.5
1
0.5
0
Non tumor
Tumor
F
CTL
DEN
DEN + 4μ8C
Clmp
Yes1
Foxo1
Pla2g4a
Prdx5
Tgfa
Epo
Axin1
Fst
Nadk
Snap29
S100a4
Kitlg
Gfra1
Ppp1r2
Cyr61
Ahr
Ccl2
Qdpr
Fas
Riox2
Epcam
Ccl3
Crim1
Hgf
Sez6l2
Il1a
Ddah1
Acvrl1
Cxcl9
Map2k6
Casp3
Pdgfb
Igsf3
Cxcl1
Pak4
Lpl
Dctn2
Nuf3
Tnfsf12
Ccl20
Fil1
Tpp1
Parp1

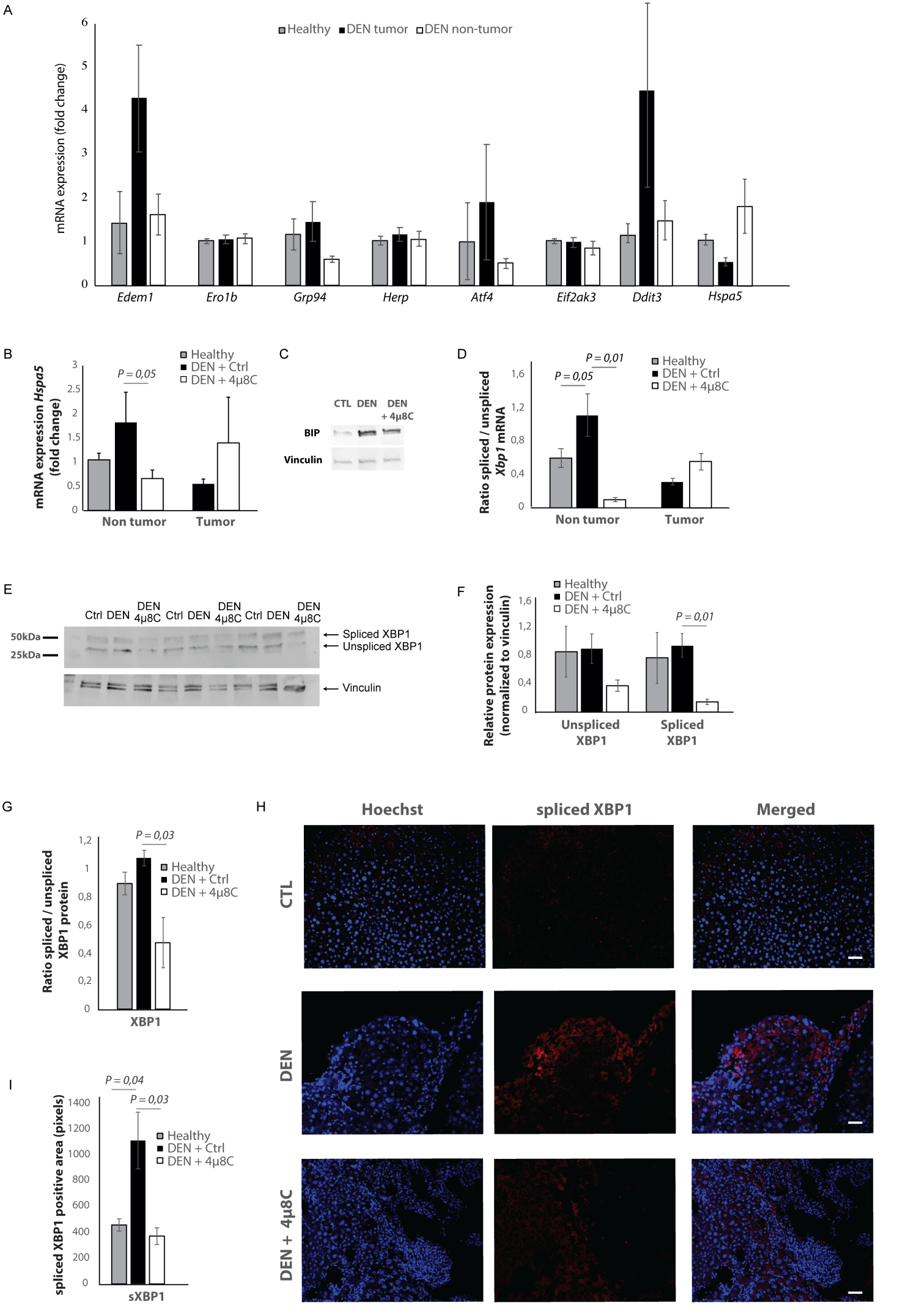
A
Healthy
DEN tumor
DEN non-tumor
mRNA expression (fold change)
Edem1
Ero1b
Grp94
Herp
Atf4
Eif2ak3
Ddit3
Hspa5
B
Healthy
DEN + Ctrl
DEN + 4µ8C
mRNA expression Hspa5 (fold change)
P = 0,05
Non tumor
Tumor
C
CTL
DEN
DEN + 4µ8C
BIP
Vinculin
D
P = 0,01
P = 0,05
Ratio spliced / unspliced Xbp1 mRNA
Non tumor
Tumor
E
Ctrl
DEN
DEN 4µ8C
50kDa
25kDa
Spliced XBP1
Unspliced XBP1
Vinculin
F
Relative protein expression (normalized to vinculin)
P = 0,01
Unspliced XBP1
Spliced XBP1
G
P = 0,03
Ratio spliced / unspliced XBP1 protein
XBP1
H
Hoechst
spliced XBP1
Merged
CTL
DEN
DEN + 4µ8C
I
P = 0,04
P = 0,03
spliced XBP1 positive area (pixels)
sXBP1

A

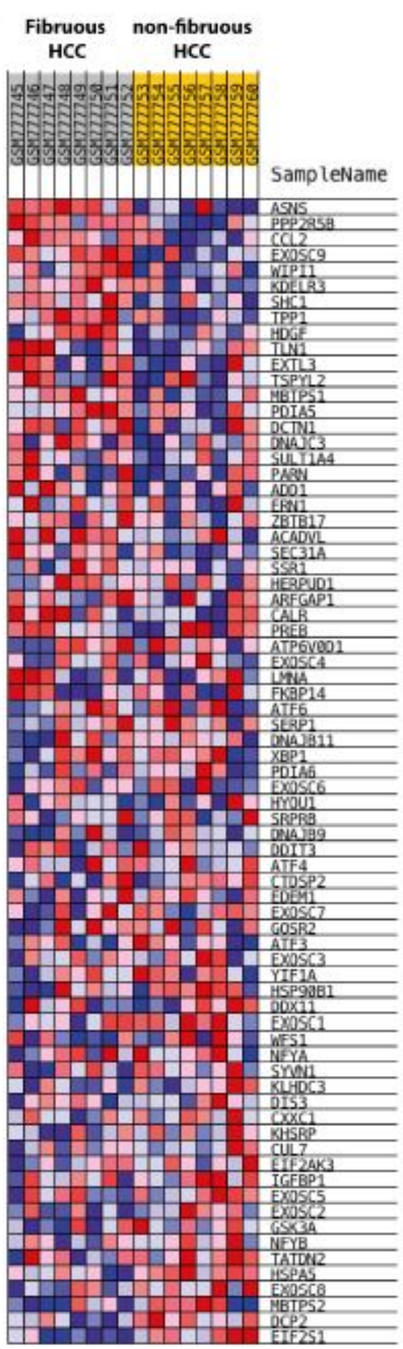
Fibruous HCC
non-fibruous HCC
GSM777745
GSM777746
GSM777747
GSM777748
GSM777749
GSM777750
GSM777751
GSM777752
GSM777753
GSM777754
GSM777755
GSM777756
GSM777757
GSM777758
GSM777759
GSM777760
SampleName
ASNS
PPP2R5B
CCL2
EXOSC9
WIPI1
KDELR3
SHC1
TPP1
HDGF
TLN1
EXTL3
TSPYL2
MBTPS1
PDIA5
DCTN1
DNAJC3
SULT1A4
PARN
ADO1
ERN1
ZBTB17
ACADVL
SEC31A
SSR1
HERPUD1
ARFGAP1
CALR
PREB
ATP6V0D1
EXOSC4
LMNA
FKBP14
ATF6
SERP1
DNAJB11
XBP1
PDIA6
EXOSC6
HYOU1
SRPRB
DNAJB9
DDIT3
ATF4
CTDSP2
EDEM1
EXOSC7
GOSR2
ATF3
EXOSC3
YIF1A
HSP90B1
DDX11
EXOSC1
WFS1
NFYA
SYNM1
KLHDC3
DIS3
CXXC1
KHSRP
CUL7
EIF2AK3
TGFBP1
EXOSC5
EXOSC2
GSK3A
NFYB
TATDN2
HSPA5
EXOSC8
MBTPS2
OCP2
EIF2S1

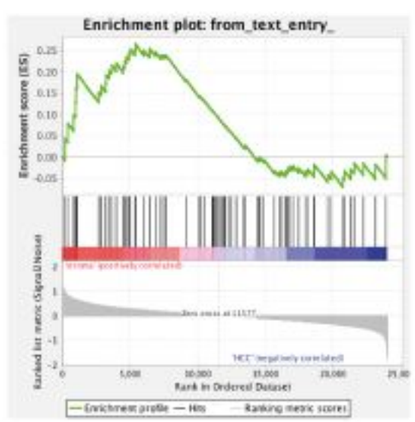
Enrichment plot: from_text_entry_
Enrichment score (ES)
Ranked list metric (Signal2Noise)
Rank in Ordered Dataset
Enrichment profile
Hits
Ranking metric scores

B

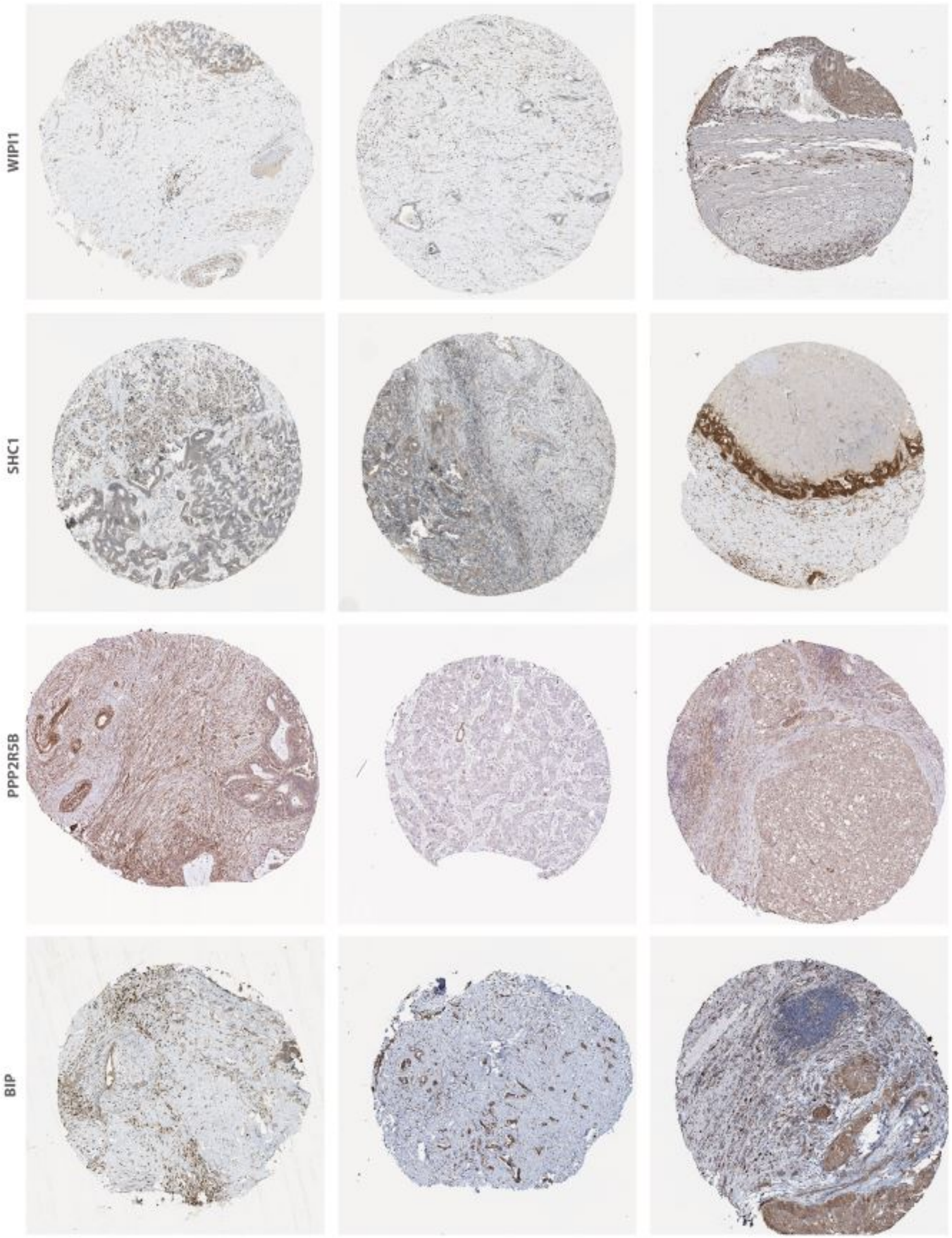
WIPI1
SHC1
PPP2R5B
BIP

C

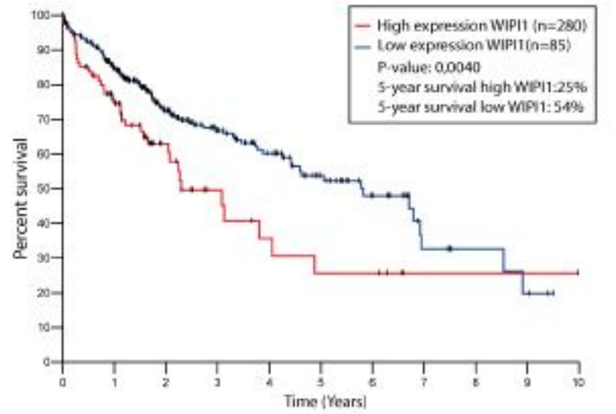
High expression WIPI1 (n=280)
Low expression WIPI1(n=85)
P-value: 0,0040
5-year survival high WIPI1:25%
5-year survival low WIPI1: 54%
Percent survival
Time (Years)

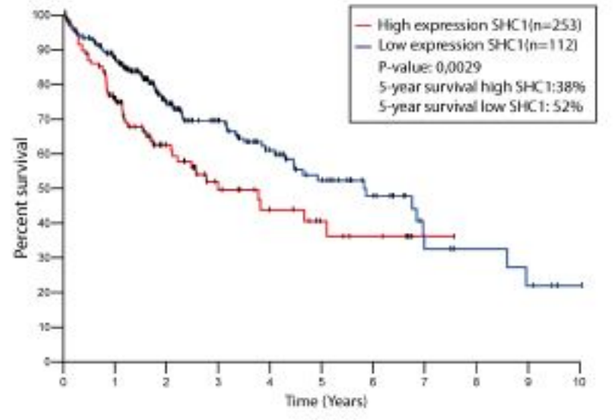
High expression SHC1(n=253)
Low expression SHC1(n=112)
P-value: 0,0029
5-year survival high SHC1:38%
5-year survival low SHC1: 52%
Percent survival
Time (Years)

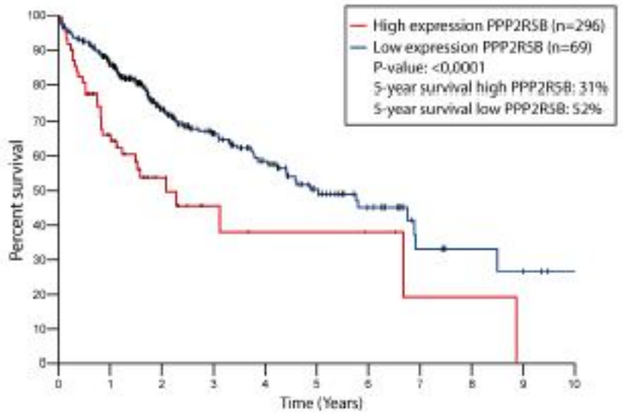
High expression PPP2R5B (n=296)
Low expression PPP2R5B (n=69)
P-value: <0,0001
5-year survival high PPP2R5B: 31%
5-year survival low PPP2R5B: 52%
Percent survival
Time (Years)

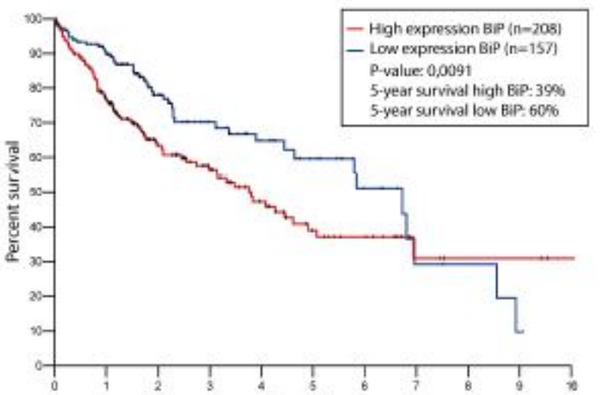
High expression BiP (n=208)
Low expression BiP (n=157)
P-value: 0,0091
5-year survival high BiP: 39%
5-year survival low BiP: 60%
Percent survival
Time (Years)

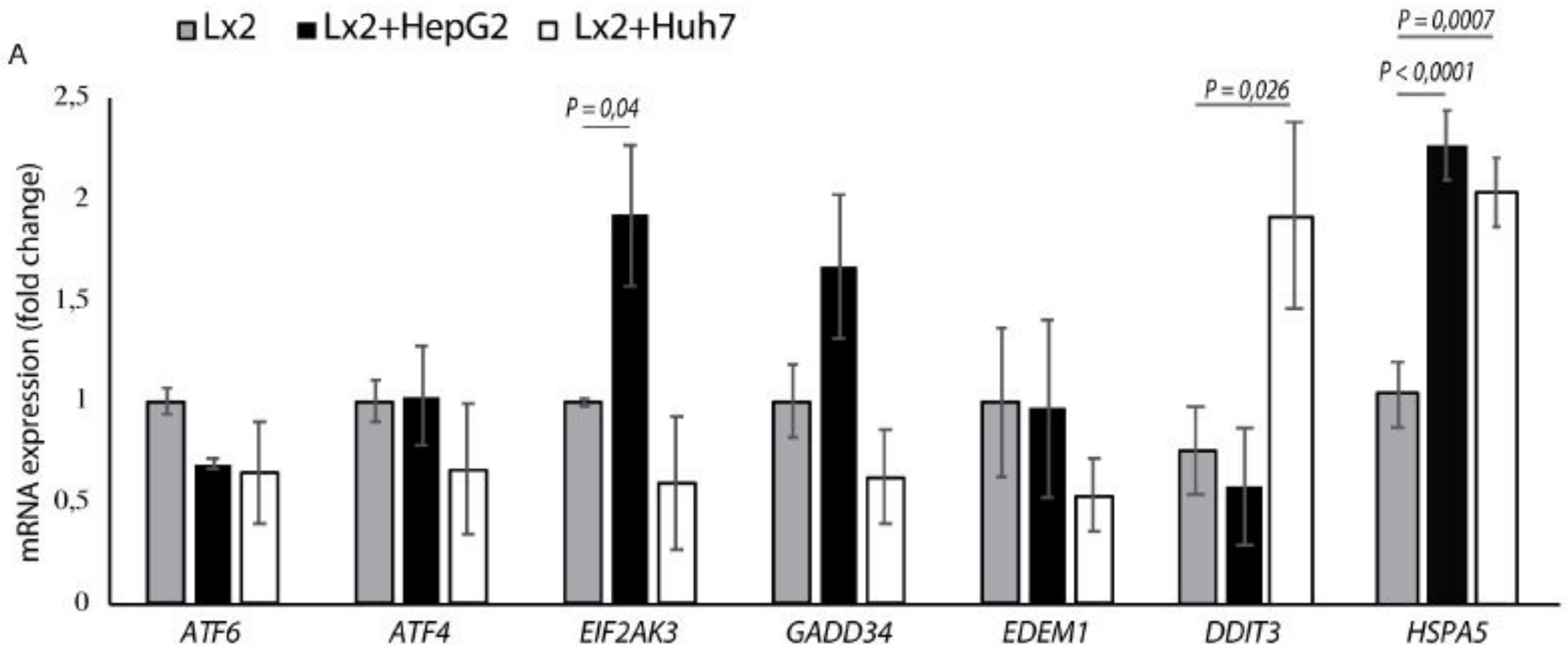
A
Lx2
Lx2+HepG2
Lx2+Huh7
mRNA expression (fold change)
P = 0,04
P = 0,026
P = 0,0007
P < 0,0001
ATF6
ATF4
EIF2AK3
GADD34
EDEM1
DDIT3
HSPA5

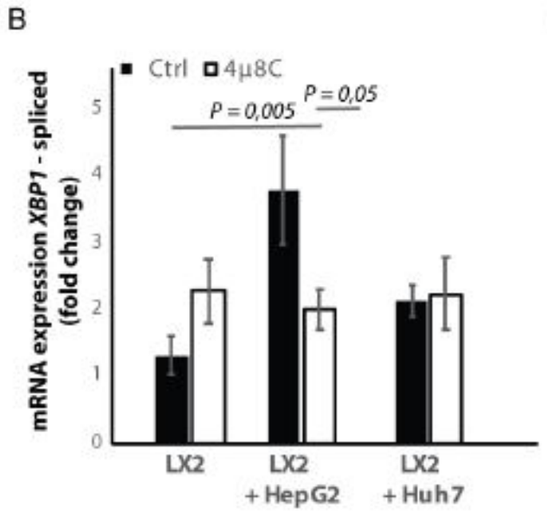
B
Ctrl
4μ8C
mRNA expression XBP1 - spliced (fold change)
P = 0,005
P = 0,05
LX2
LX2 + HepG2
LX2 + Huh7

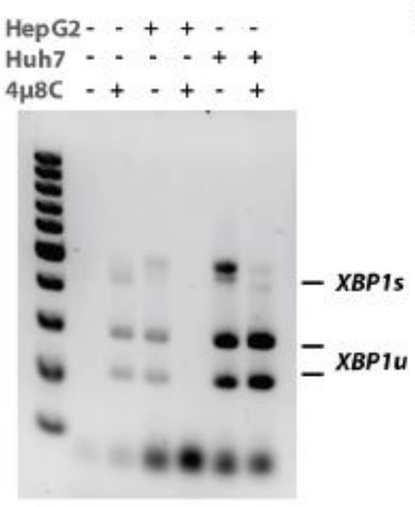
C
HepG2
Huh7
4μ8C
XBP1s
XBP1u

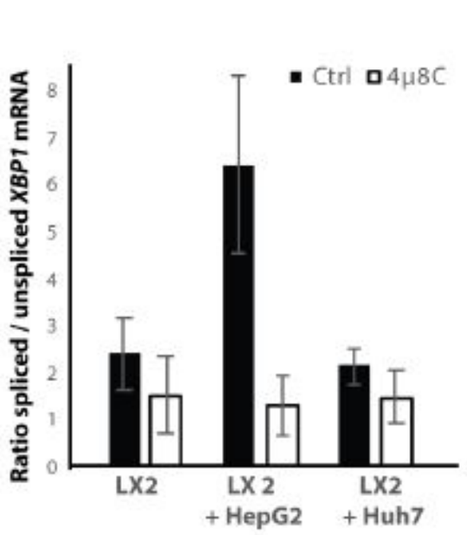
D
Ctrl
4μ8C
Ratio spliced / unspliced XBP1 mRNA
LX2
LX 2 + HepG2
LX2 + Huh7

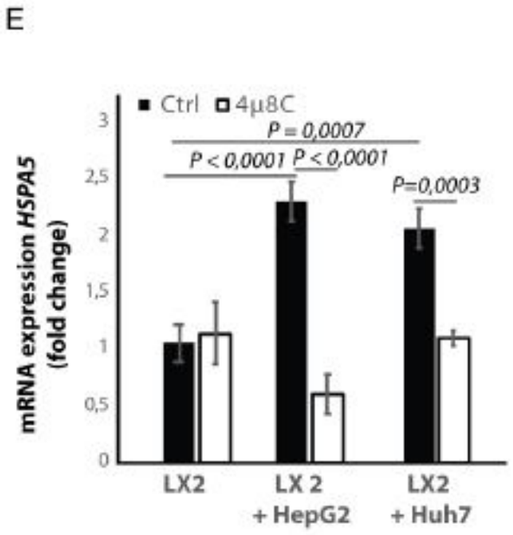
E
Ctrl
4μ8C
P = 0,0007
P < 0,0001
P < 0,0001
P=0,0003
mRNA expression HSPA5 (fold change)
LX2
LX 2 + HepG2
LX2 + Huh7


F
HepG2
Huh7
4μ8C
p-IRE1α
Vinculin

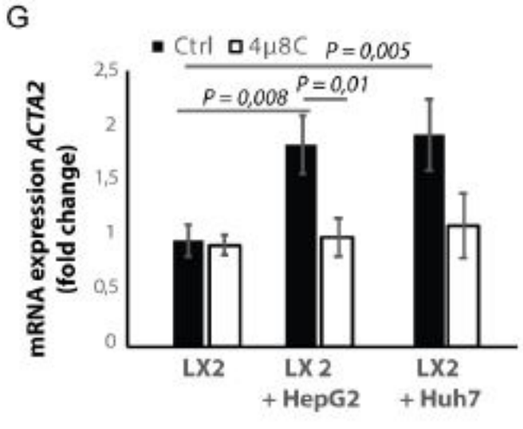
G
Ctrl
4μ8C
P = 0,005
P = 0,008
P = 0,01
mRNA expression ACTA2 (fold change)
LX2
LX 2 + HepG2
LX2 + Huh7

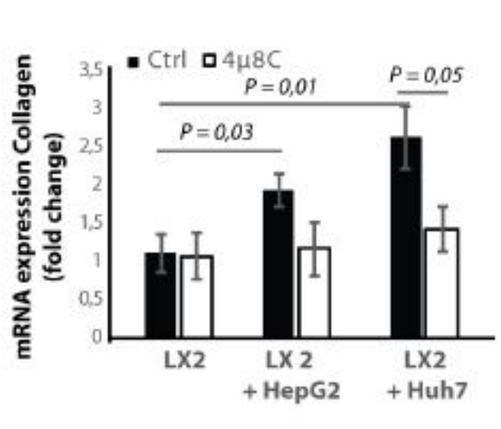
H
Ctrl
4μ8C
P = 0,01
P = 0,05
P = 0,03
mRNA expression Collagen (fold change)
LX2
LX 2 + HepG2
LX2 + Huh7

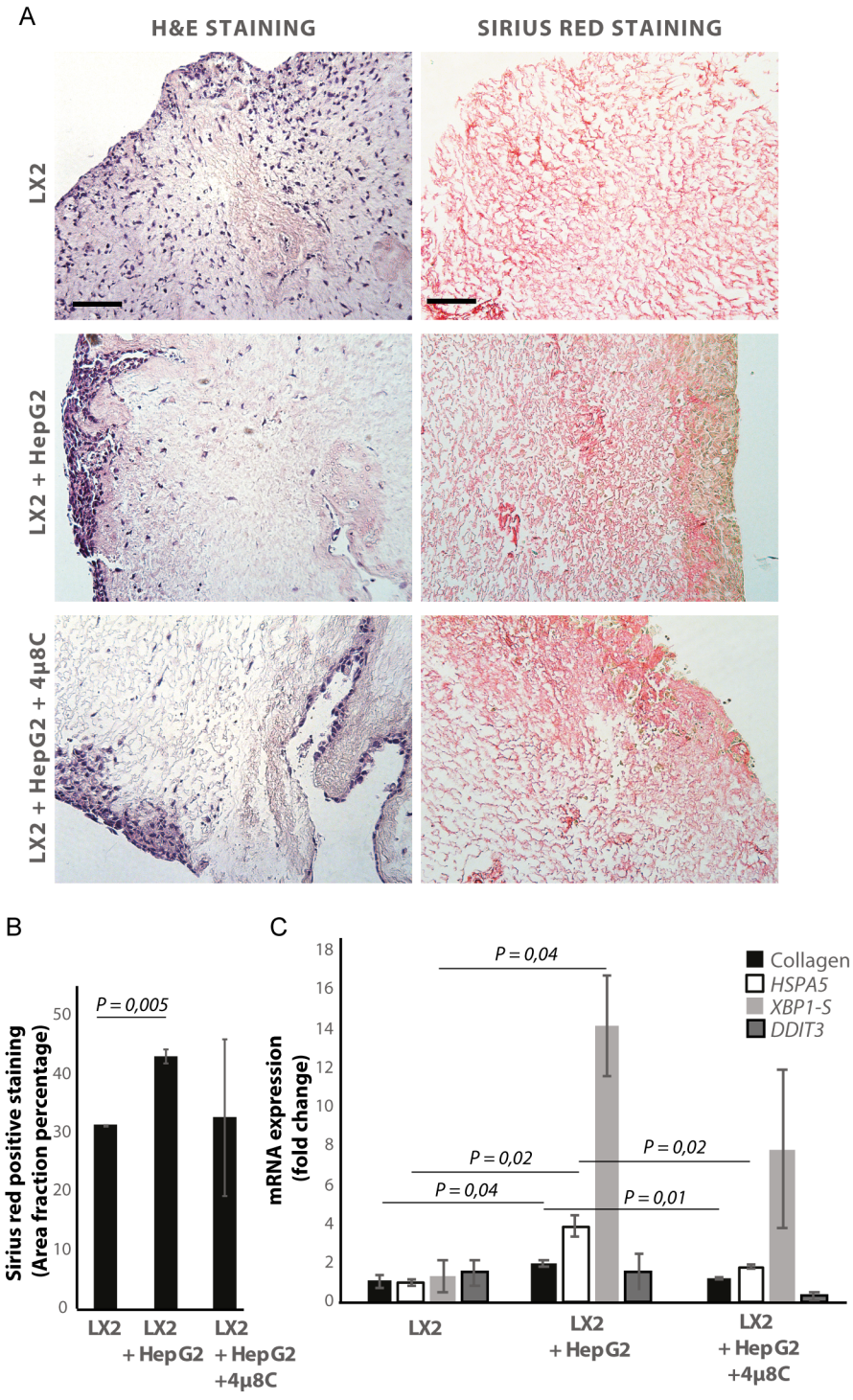
A
H&E STAINING
SIRIUS RED STAINING
LX2
LX2 + HepG2
LX2 + HepG2 + 4µ8C
B
Sirius red positive staining (Area fraction percentage)
P = 0,005
0
10
20
30
40
50
LX2
LX2 + HepG2
LX2 + HepG2 +4µ8C
C
mRNA expression (fold change)
P = 0,04
P = 0,02
P = 0,04
P = 0,02
P = 0,01
0
2
4
6
8
10
12
14
16
18
Collagen
HSPA5
XBP1-S
DDIT3
LX2
LX2 + HepG2
LX2 + HepG2 +4µ8C

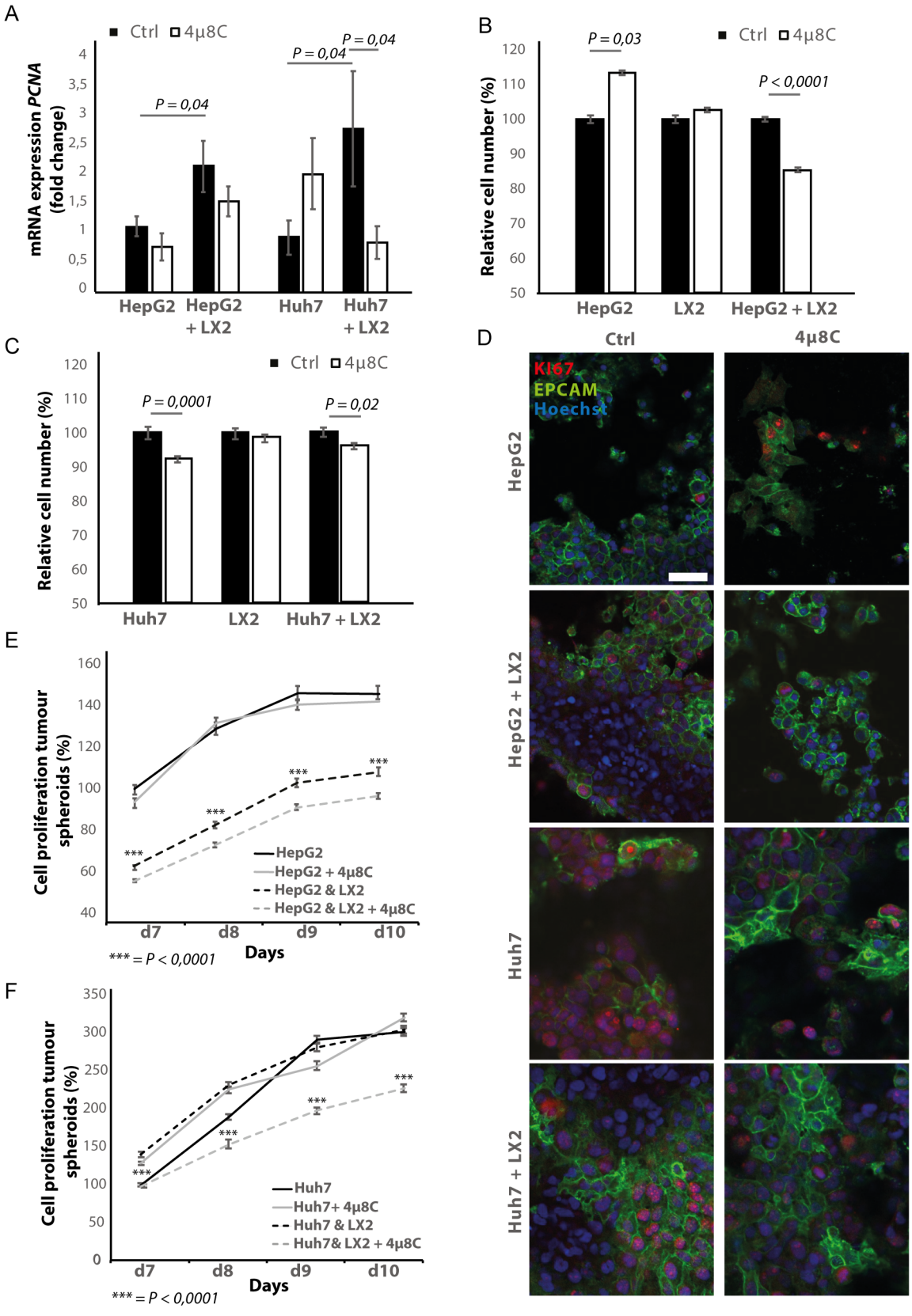
A
Ctrl
4µ8C
mRNA expression PCNA (fold change)
P = 0,04
P = 0,04
P = 0,04
HepG2
HepG2 + LX2
Huh7
Huh7 + LX2
B
Ctrl
4µ8C
Relative cell number (%)
P = 0,03
P < 0,0001
HepG2
LX2
HepG2 + LX2
C
Ctrl
4µ8C
Relative cell number (%)
P = 0,0001
P = 0,02
Huh7
LX2
Huh7 + LX2
D
Ctrl
4µ8C
KI67
EPCAM
Hoechst
HepG2
HepG2 + LX2
Huh7
Huh7 + LX2
E
Cell proliferation tumour spheroids (%)
HepG2
HepG2 + 4µ8C
HepG2 & LX2
HepG2 & LX2 + 4µ8C
d7
d8
d9
d10
Days
*** = P < 0,0001
F
Cell proliferation tumour spheroids (%)
Huh7
Huh7+ 4µ8C
Huh7 & LX2
Huh7& LX2 + 4µ8C
d7
d8
d9
d10
Days
*** = P < 0,0001

A

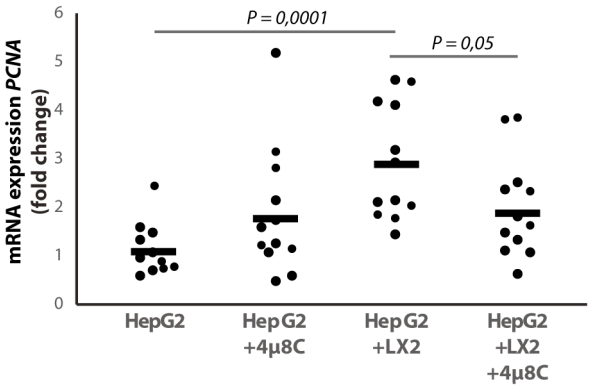
P = 0,0001
P = 0,05
mRNA expression PCNA (fold change)
0
1
2
3
4
5
6
HepG2
HepG2 +4µ8C
HepG2 +LX2
HepG2 +LX2 +4µ8C

B

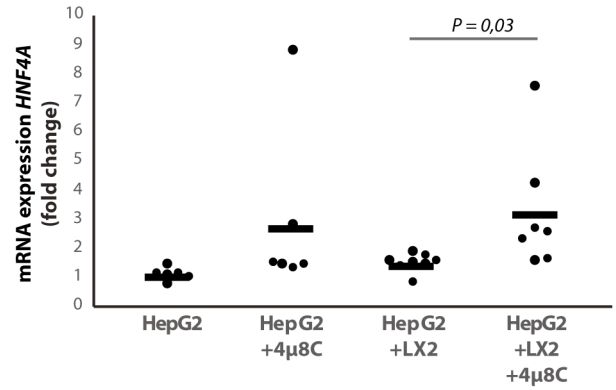
P = 0,03
mRNA expression HNF4A (fold change)
0
1
2
3
4
5
6
7
8
9
10
HepG2
HepG2 +4µ8C
HepG2 +LX2
HepG2 +LX2 +4µ8C

C

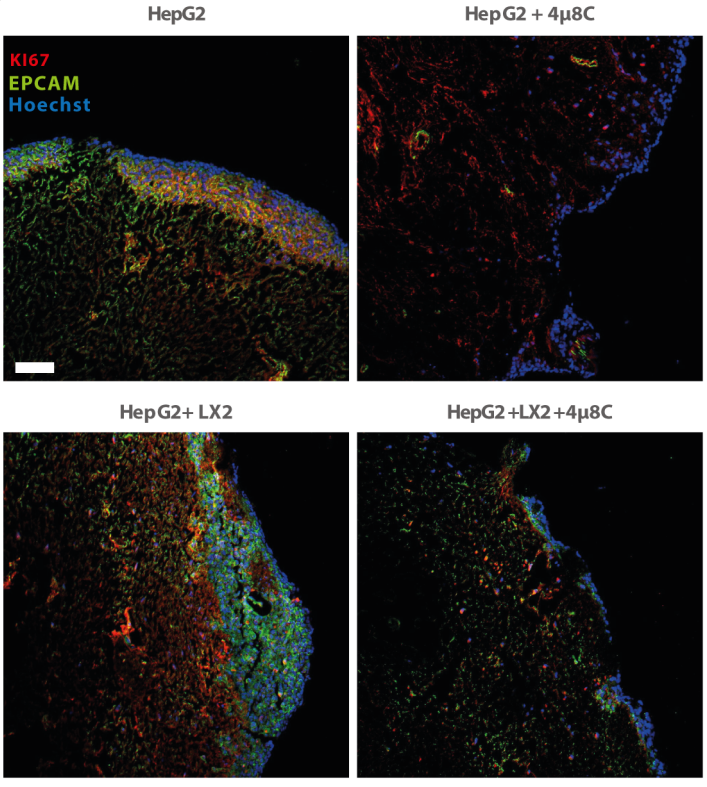
HepG2
HepG2 + 4µ8C
KI67
EPCAM
Hoechst
HepG2+ LX2
HepG2 +LX2 +4µ8C

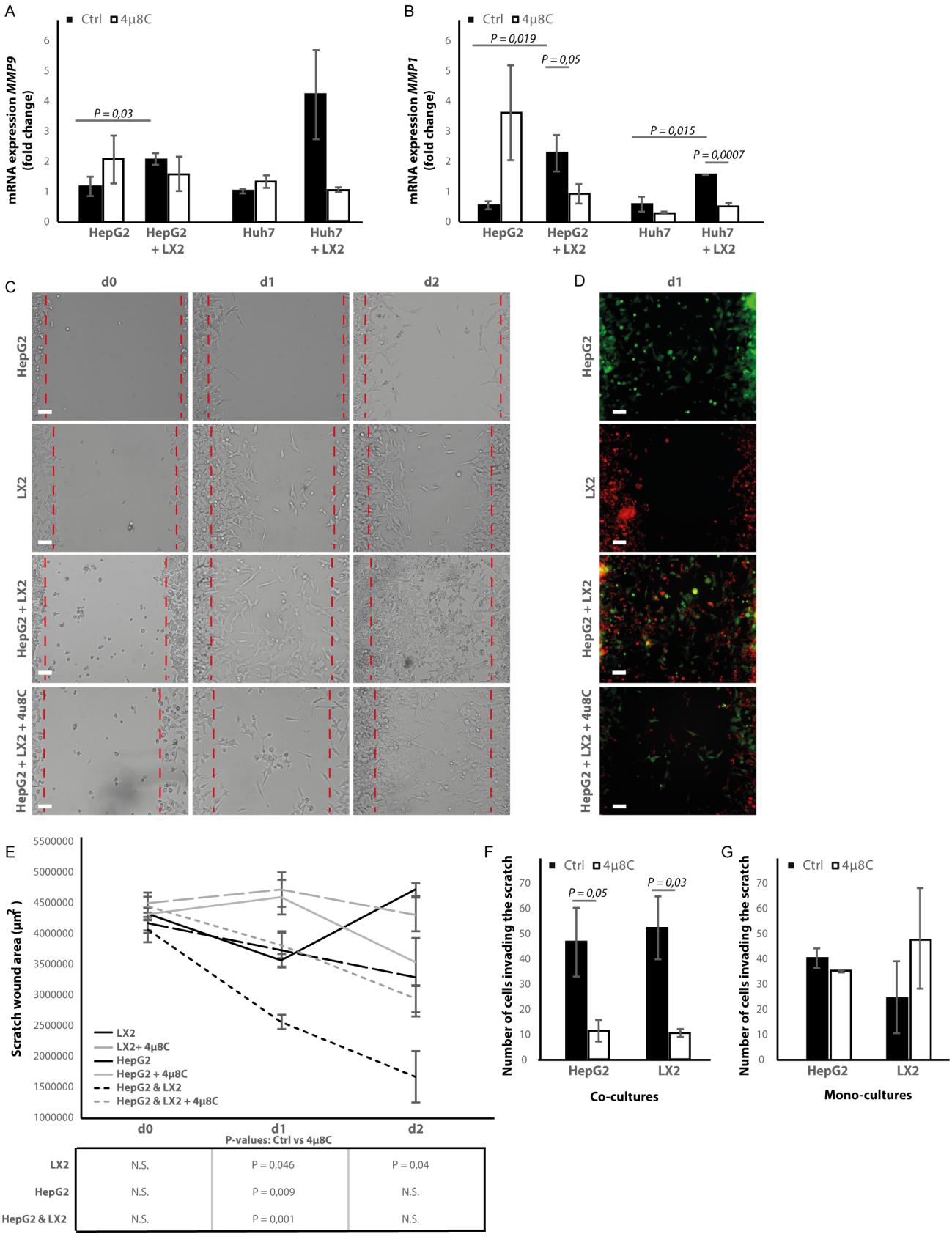
A
Ctrl
4µ8C
mRNA expression MMP9 (fold change)
P = 0,03
HepG2
HepG2 + LX2
Huh7
Huh7 + LX2
B
mRNA expression MMP1 (fold change)
P = 0,019
P = 0,05
P = 0,015
P = 0,0007
C
d0
d1
d2
HepG2
LX2
HepG2 + LX2
HepG2 + LX2 + 4u8C
D
E
Scratch wound area (µm²)
LX2
LX2+ 4µ8C
HepG2
HepG2 + 4µ8C
HepG2 & LX2
HepG2 & LX2 + 4µ8C
P-values: Ctrl vs 4µ8C
LX2 N.S. P = 0,046 P = 0,04
HepG2 N.S. P = 0,009 N.S.
HepG2 & LX2 N.S. P = 0,001 N.S.
F
Number of cells invading the scratch
P = 0,05
P = 0,03
Co-cultures
G
Mono-cultures

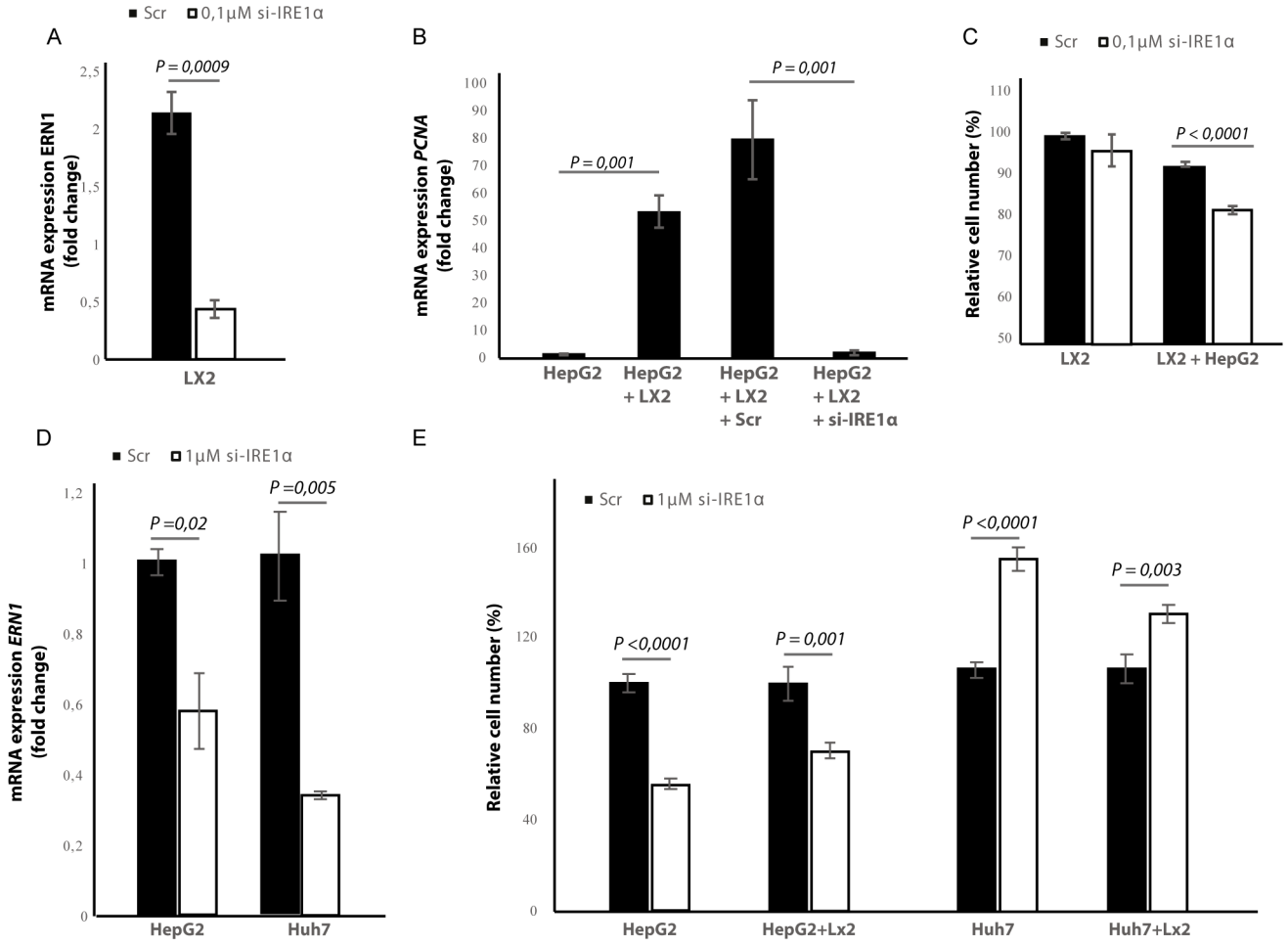
A
■ Scr □ 0,1µM si-IRE1α
mRNA expression ERN1 (fold change)
P = 0,0009
LX2
B
mRNA expression PCNA (fold change)
P = 0,001
P = 0,001
HepG2
HepG2 + LX2
HepG2 + LX2 + Scr
HepG2 + LX2 + si-IRE1α
C
■ Scr □ 0,1µM si-IRE1α
Relative cell number (%)
P < 0,0001
LX2
LX2 + HepG2
D
■ Scr □ 1µM si-IRE1α
mRNA expression ERN1 (fold change)
P =0,02
P =0,005
HepG2
Huh7
E
■ Scr □ 1µM si-IRE1α
Relative cell number (%)
P <0,0001
P = 0,001
P <0,0001
P = 0,003
HepG2
HepG2+Lx2
Huh7
Huh7+Lx2

A

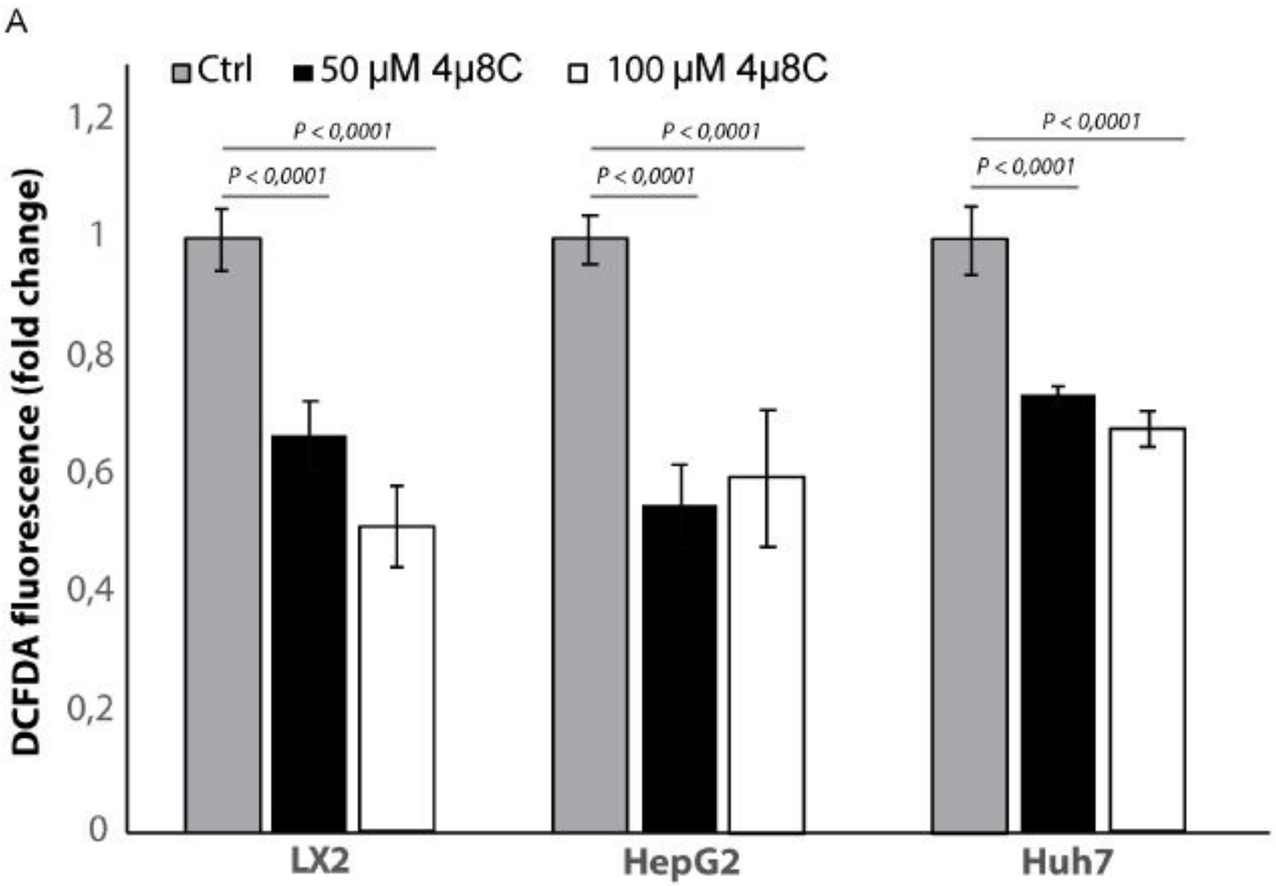
Ctrl
50 µM 4µ8C
100 µM 4µ8C
DCFDA fluorescence (fold change)
1,2
1
0,8
0,6
0,4
0,2
0
P < 0,0001
P < 0,0001
P < 0,0001
P < 0,0001
P < 0,0001
P < 0,0001
LX2
HepG2
Huh7

B

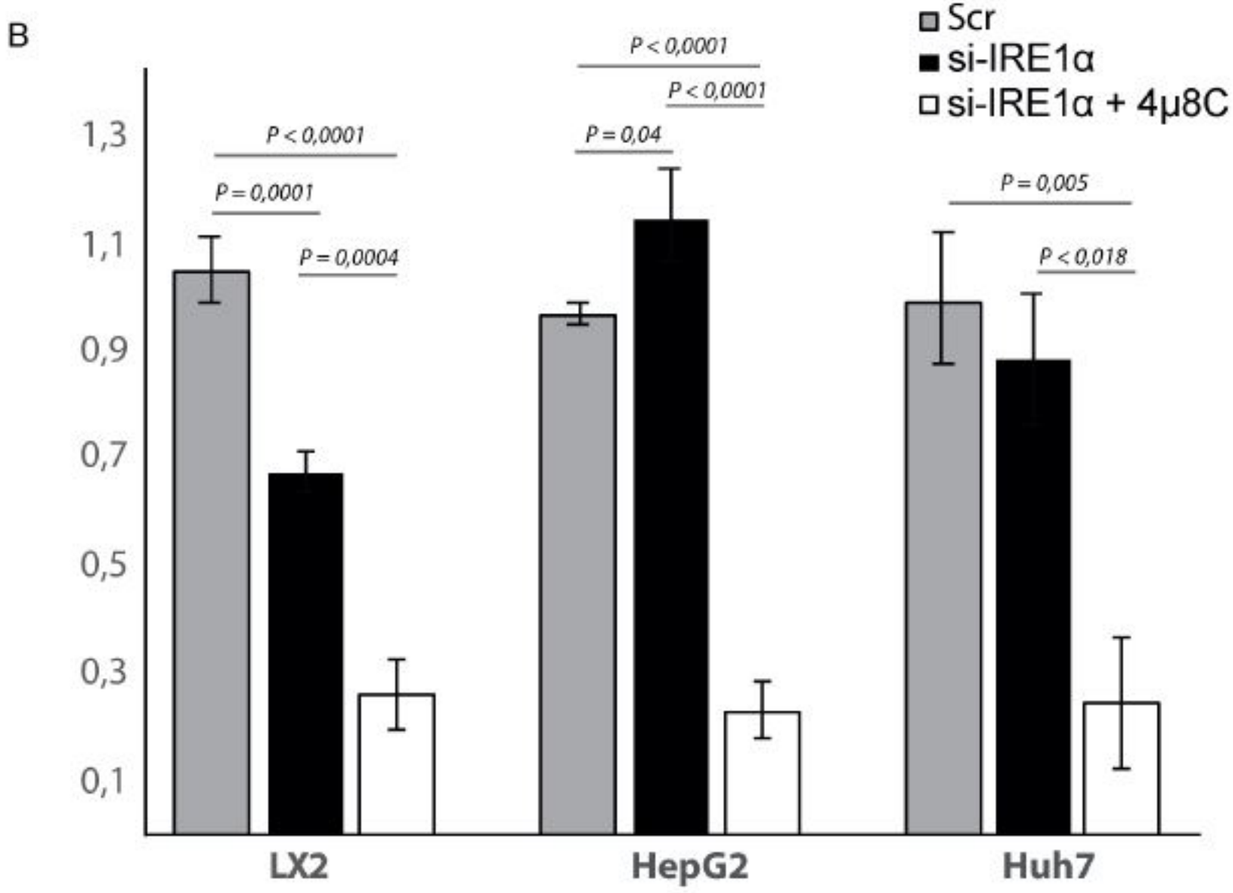
Scr
si-IRE1α
si-IRE1α + 4µ8C
1,3
1,1
0,9
0,7
0,5
0,3
0,1
P < 0,0001
P = 0,0001
P = 0,0004
P < 0,0001
P < 0,0001
P = 0,04
P = 0,005
P < 0,018
LX2
HepG2
Huh7

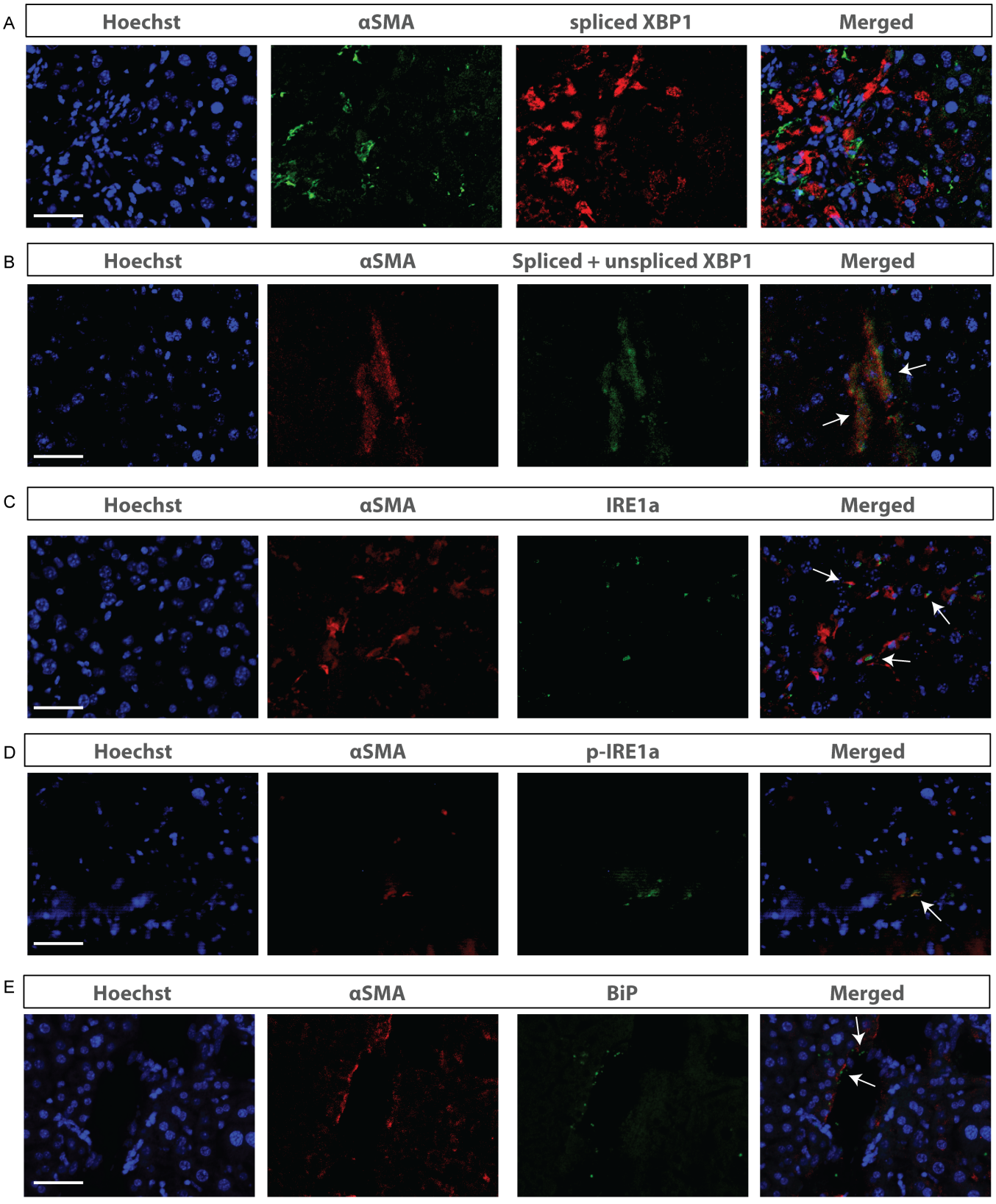
A
Hoechst
αSMA
spliced XBP1
Merged
B
Hoechst
αSMA
Spliced + unspliced XBP1
Merged
C
Hoechst
αSMA
IRE1a
Merged
D
Hoechst
αSMA
p-IRE1a
Merged
E
Hoechst
αSMA
BiP
Merged

A

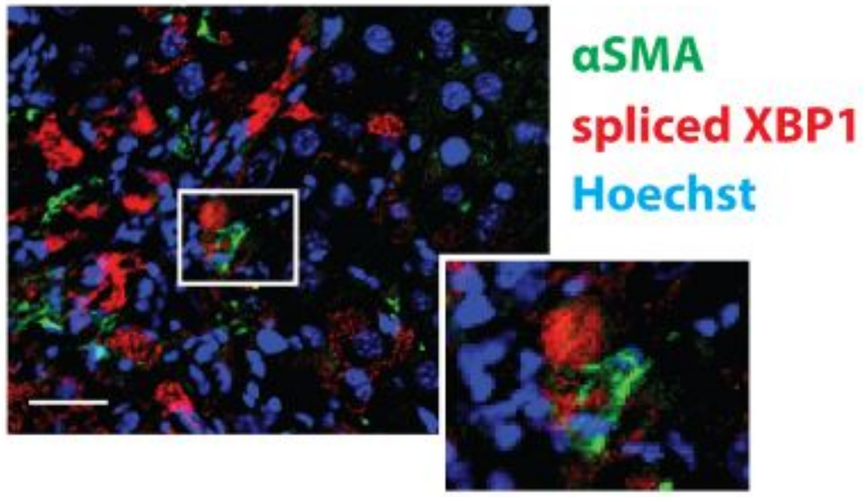
αSMA
spliced XBP1
Hoechst

B

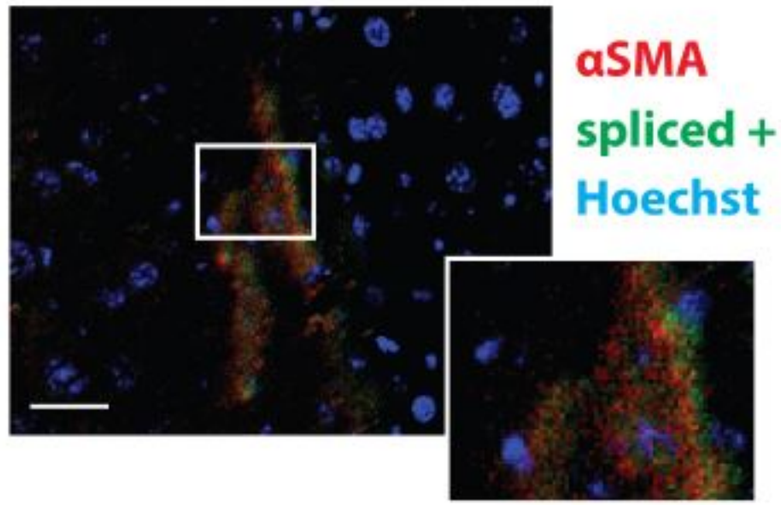
αSMA
spliced + unspliced XBP1
Hoechst

C

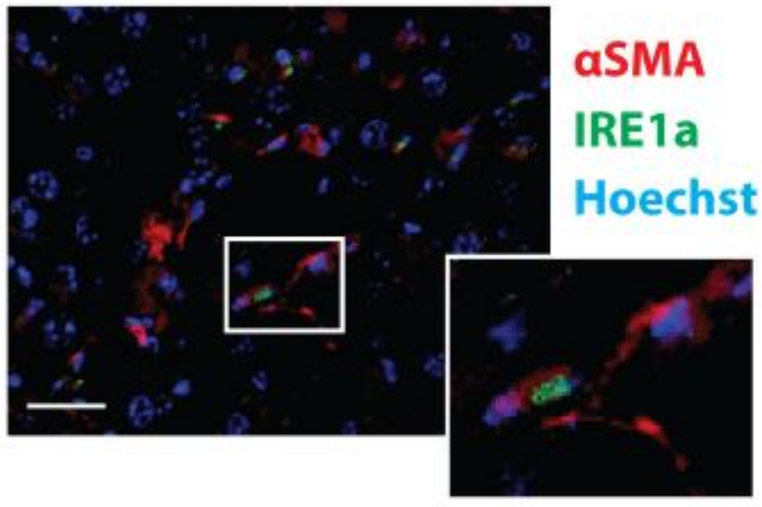
αSMA
IRE1a
Hoechst

D

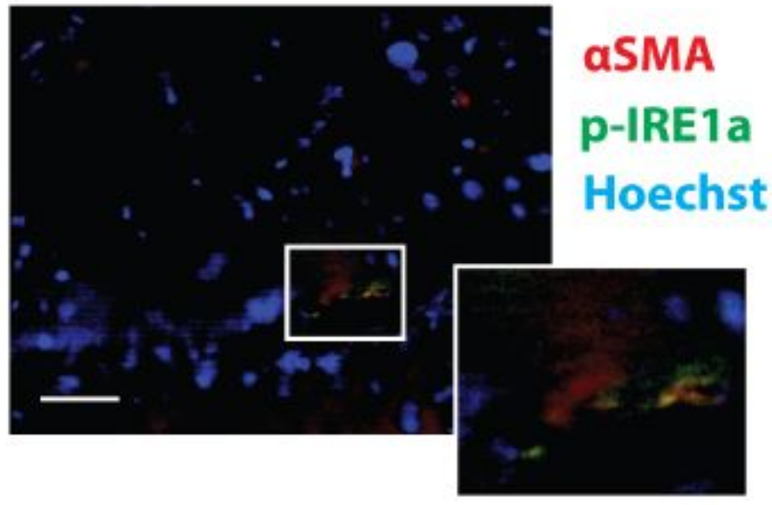
αSMA
p-IRE1a
Hoechst

E

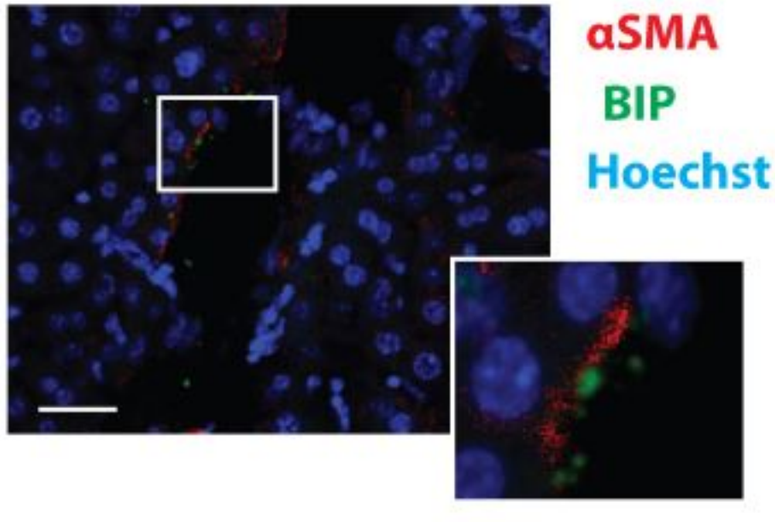
αSMA
BIP
Hoechst

F

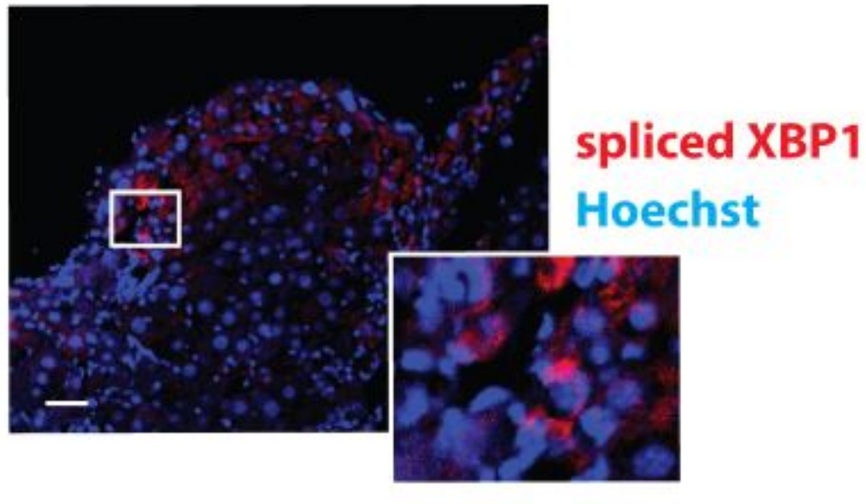
spliced XBP1
Hoechst

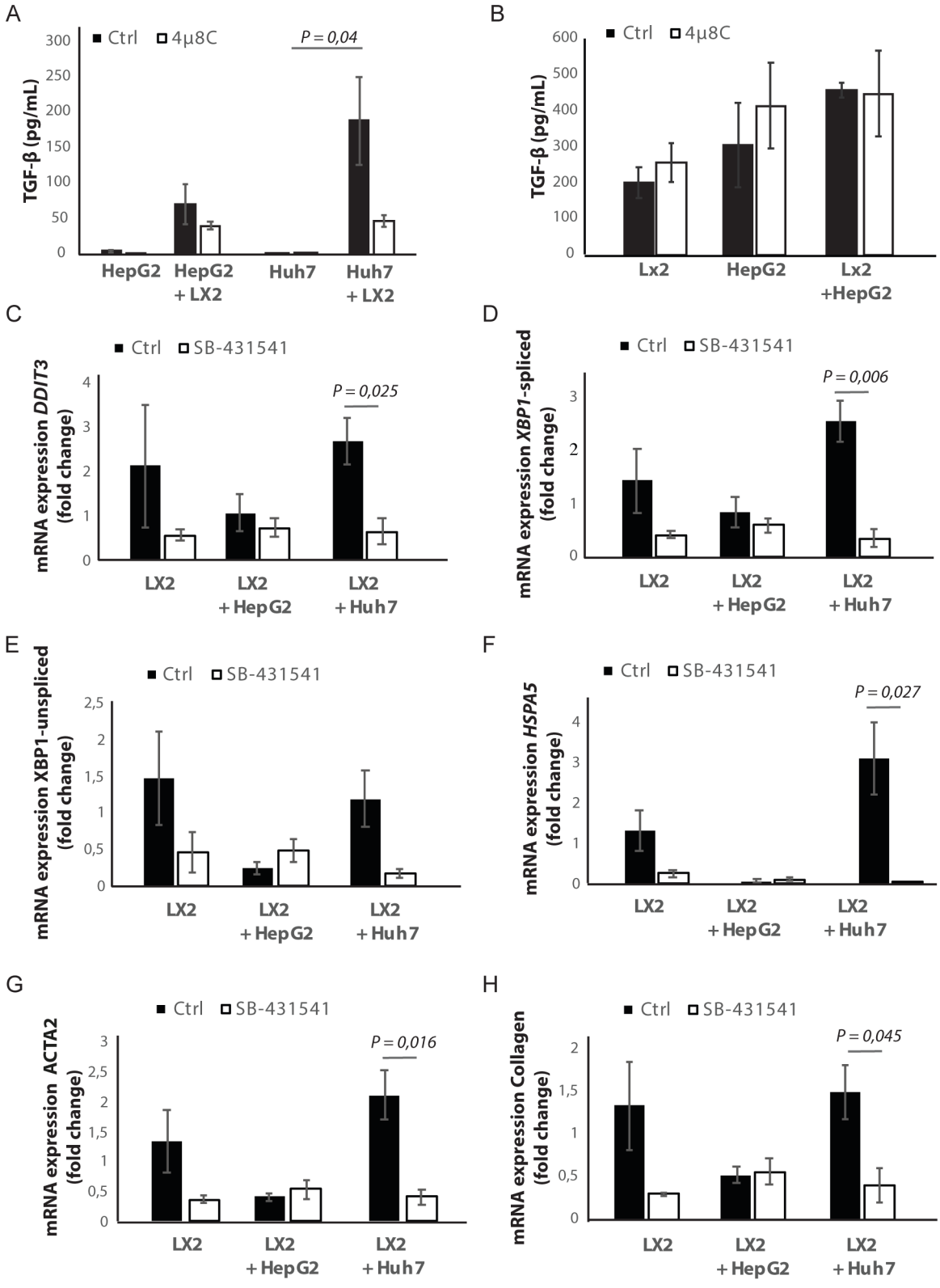
A
Ctrl
4µ8C
P = 0,04
TGF-β (pg/mL)
300
250
200
150
100
50
0
HepG2
HepG2 + LX2
Huh7
Huh7 + LX2
B
Ctrl
4µ8C
TGF-β (pg/mL)
600
500
400
300
200
100
0
Lx2
HepG2
Lx2 +HepG2
C
Ctrl
SB-431541
P = 0,025
mRNA expression DDIT3 (fold change)
4
3
2
1
0
LX2
LX2 + HepG2
LX2 + Huh7
D
Ctrl
SB-431541
P = 0,006
mRNA expression XBP1-spliced (fold change)
3
2
1
0
LX2
LX2 + HepG2
LX2 + Huh7
E
Ctrl
SB-431541
mRNA expression XBP1-unspliced (fold change)
2,5
2
1,5
1
0,5
0
LX2
LX2 + HepG2
LX2 + Huh7
F
Ctrl
SB-431541
P = 0,027
mRNA expression HSPA5 (fold change)
4
3
2
1
0
LX2
LX2 + HepG2
LX2 + Huh7
G
Ctrl
SB-431541
P = 0,016
mRNA expression ACTA2 (fold change)
3
2,5
2
1,5
1
0,5
0
LX2
LX2 + HepG2
LX2 + Huh7
H
Ctrl
SB-431541
P = 0,045
mRNA expression Collagen (fold change)
2
1,5
1
0,5
0
LX2
LX2 + HepG2
LX2 + Huh7

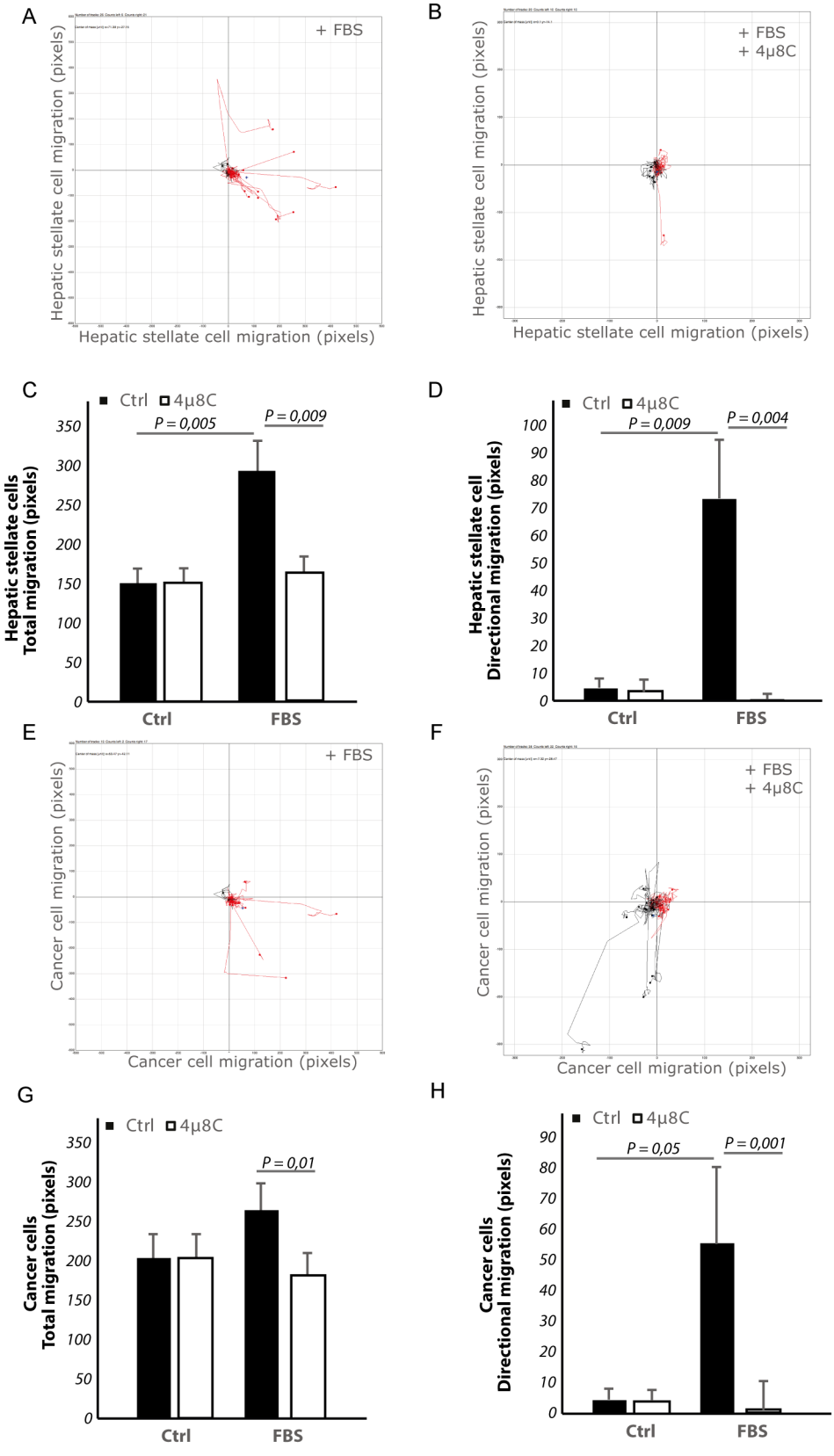
A
+ FBS
Hepatic stellate cell migration (pixels)
Hepatic stellate cell migration (pixels)
B
+ FBS
+ 4µ8C
Hepatic stellate cell migration (pixels)
Hepatic stellate cell migration (pixels)
C
Ctrl
4µ8C
P = 0,005
P = 0,009
Hepatic stellate cells
Total migration (pixels)
350
300
250
200
150
100
50
0
Ctrl
FBS
D
Ctrl
4µ8C
P = 0,009
P = 0,004
Hepatic stellate cell
Directional migration (pixels)
100
90
80
70
60
50
40
30
20
10
0
Ctrl
FBS
E
+ FBS
Cancer cell migration (pixels)
Cancer cell migration (pixels)
F
+ FBS
+ 4µ8C
Cancer cell migration (pixels)
Cancer cell migration (pixels)
G
Ctrl
4µ8C
P = 0,01
Cancer cells
Total migration (pixels)
350
300
250
200
150
100
50
0
Ctrl
FBS
H
Ctrl
4µ8C
P = 0,05
P = 0,001
Cancer cells
Directional migration (pixels)
90
80
70
60
50
40
30
20
10
0
Ctrl
FBS

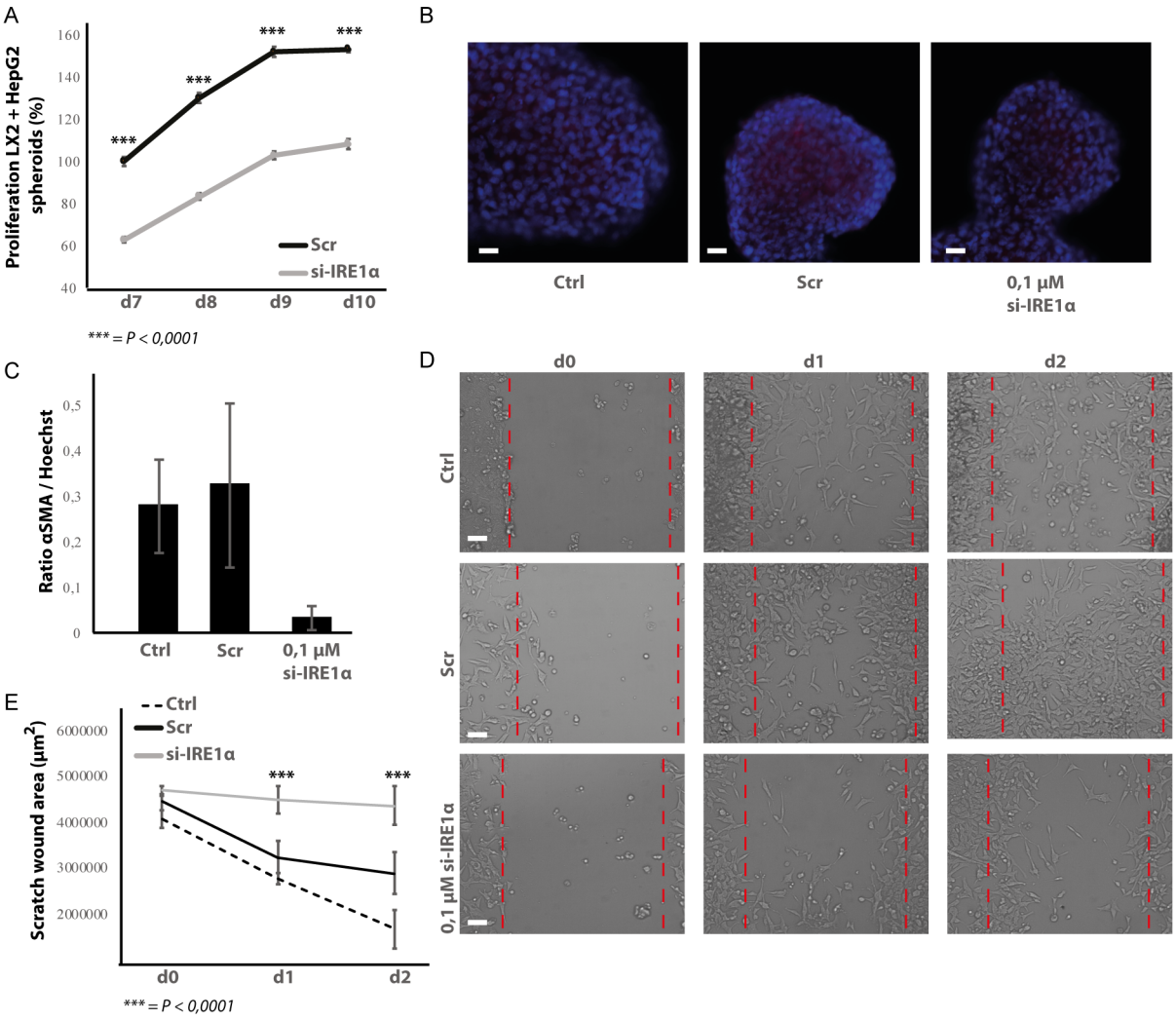
A
Proliferation LX2 + HepG2 spheroids (%)
160
140
120
100
80
60
40
***
***
***
***
Scr
si-IRE1α
d7
d8
d9
d10
*** = P < 0,0001
B
Ctrl
Scr
0,1 µM si-IRE1α
C
Ratio αSMA / Hoechst
0,5
0,4
0,3
0,2
0,1
0
Ctrl
Scr
0,1 µM si-IRE1α
D
d0
d1
d2
Ctrl
Scr
0,1 µM si-IRE1α
E
Ctrl
Scr
si-IRE1α
Scratch wound area (µm²)
6000000
5000000
4000000
3000000
2000000
***
***
d0
d1
d2
*** = P < 0,0001